Experimental study of wave trains generated by vertical bed movements

Dominic E. Reeve , Jose Horrillo-Caraballo , Harshinie Karunarathna , Xin Wang [*]

Coastal Engineering Research Group, Faculty of Science and Engineering, Swansea University, Swansea SA1 8EN, United Kingdom

ABSTRACT

Laboratory experiments were conducted to explore the wave trains generated by vertical bed movements. The investigation consisted of 32 cases, involving four different water depths with unimodal and bimodal bed movements. Water surface displacement was measured using gauges positioned along a 30m long tank. A PIV system was set up to provide detailed measurement of the fluid velocity field in the vicinity of the bed movement. Generally, a unimodal movement generated a solitary-like wave, followed by a trailing sequence of waves. A bimodal bed movement induced a more complex flow field, with both the first and second extrema being significant. New analytical solutions have been derived, enabling the calculation of velocity fields. The nature of the wave generation and propagation were characterised using the disturbance-amplitude scale (α) and disturbance-size scale (δ). The applicability of linear theory was investigated, by validating the linear solutions of the generated waves against the experimental observations. For $\alpha \leq 0.25$, the analytical solutions were in good agreement with observations of the free surface shape, flow field and wave elevation history. For $\alpha \geq 0.5$, non-linearity became more pronounced, and the analytical solutions were only capable of reasonably estimating the amplitude of the first extremum in the vicinity of the moving bed. The initial crest maintained its amplitude and shape more effectively in crest-leading waves, whereas the leading trough decayed significantly in trough-leading waves. Non-linear phenomena were observed, such as wave breaking, air entrapment and twisted free surface. Bimodal bed movements with $\alpha \geq 0.5$ generated large, steep crests immediately following the initial trough in trough-leading waves.

1. Introduction

Seabed movements are one of the main causes of long period ocean waves such as tsunamis. The characteristics of tsunamis vary depending on the details of the seabed movement (Synolakis and Bernard, 2006). To study tsunami-like waves, laboratory experiments have been conducted with various wave generation devices, such as horizontal pistons (Schimmels et al. 2016); vertical pistons at the seabed (Jamin et al., 2015); moving blocks (Whittaker et al. 2017); collapsing sediment mounds (Enet & Grilli 2007); air pumps (Rossetto et al. 2011); suspended plungers (Yim et al., 2008). Real-world tsunamis, especially seismic tsunamis, typically propagate as wave trains. However, many laboratory devices generated solitary waves, lacking accurate replication of the fundamental mechanisms (Madsen et al., 2008). Seismic tsunamis are primarily generated by the vertical movement component of multi-directional seabed movements (Satake and Tanioka, 1999). Compared with the long wave period of a seismic tsunami, the short duration of the bed movement allows it to be considered as

instantaneous, (Jamin et al., 2015). Thus, a vertical bed movement can be used as an idealised model to represent seabed earthquakes for investigating wave generation.

An early example of this approach was the pioneering study by Hammack (1972), who conducted laboratory experiments of the waves generated by a vertically moving piston in a wave tank. Hammack (1972) also derived linear solutions for the wave elevation histories, which were generally applicable for a rapid bed movement with a small stroke. Braddock et al (1973) showed that a vertical bed movement would generate a non-dispersive wave front followed by a dispersive wave train. Using the same linear solution, Hayir (2004) explored the influence of water depth on the amplitudes of the generated waves. To consider the non-linearity during wave generation and propagation, non-linear models, such as the Boussinesq model, were established, achieving good results (Fuhrman and Madsen, 2009). Lynett et al. (2002) derived a depth-averaged solution based on highly nonlinear and weakly dispersive wave equations, to study the wave propagation to the shoreline and run-up. Depth-averaged non-hydrostatic models have also been proposed, exhibiting comparable accuracy with the Boussinesq

---

Nomenclature

h	water depth above the wooden frame
d	local water depth at a specific point
WG	wave gauges
UM	unimodal bed movement
UM-L/UM-R	unimodal bed movement with solely the left segment/ right segment
UM-D	unimodal bed movement with both segments moving simultaneously towards the same direction
CL/ TL	cases with the generated waves leaded by a crest/trough
BM	bimodal bed movement with the two segments moving vertically towards different directions
η_1, η_2	first and second extremum of the generated wave train, respectively
$t_{\eta1}, t_{\eta2}$	peak times; time instants correspond to η_1 and η_2, respectively
η_0	wave height for the first wave cycle, $\eta_0 = |\eta_1| + |\eta_2|$
t_a	arrival time; the instant when the rising (or falling) water level first exceeds $0.05\eta_1$
$T_{\eta1}$	first half-period; duration between t_a and the instant when the water elevation first crosses the still water level
$T_{\eta2}$	second half-period; duration between the instants of the water elevation crosses the still water level for the first and second time
T	period of the leading wave cycle; $T = T_{\eta1} + T_{\eta2}$
$\bar{c}$	wave celerity at each wave gauge, calculated by interpolation
L	wavelength of the leading wave, $L = \bar{c} \times T$
ζ_0	maximum distance of the bed movement
ζ	displacement of the moving bed
T_0	duration of the bed movement
t_c	characteristic time (the time that the bed reaches 2/3 of ζ_0)
α	disturbance-amplitude scale; $\alpha = \zeta_0/h$
δ	disturbance-size scale; $\delta = b/h$
b	half of the length of the moving seabed segment for unimodal movements
b_1, b_2	half widths of the left and right seabed segments for bimodal movements, respectively
$t_c\sqrt{gh}/b$	time size parameter
η	water surface displacement
$\widetilde{\overline{\eta}}$	water surface displacement, after Fourier and Laplace transforms
ϕ	velocity potential
$\widetilde{\overline{\phi}}$	velocity potential, after Fourier and Laplace transforms
x	distance to the centre of the moving bed segment
k	distance to the centre of the moving bed segment, transferred from x by Fourier transform
t	time
s	time, transferred from t by Laplace transform
$\mathscr{H}()$	Heaviside function
ω	angular speed, defined by $\omega^2 = gk \tanh kh$
κ	parameter used in the linear solutions of the generated wave, $\kappa = \pi/T_0$
Ur	Ursell number

models (Tjandra and Pudjaprasetya, 2015). Recently, Shen et al. (2022) extended the linear solutions to account for the movement of multiple bed segments. However, while the analytical approaches exhibited satisfactory accuracy in predicting the wave elevation histories, measurements and corresponding comparisons with velocity fields were lacking. Additionally, the region of applicability of linear theory has not been specified precisely.

Apart from the experiments of Hammack (1972), limited efforts have been paid to the experimental research of wave generation by vertical seabed movement. Notable examples include the studies by Lu et al. (2017) who developed a 'bottom-tilting' wave maker, which rotated a large portion of the tank's bottom around a hinge, generating waves with the wavelength considerably longer than the effective wavelength of solitary waves with the same amplitude; and Jamin et al. (2015) who adopted an upward-moving piston at the bottom of a circular wave basin, using a Particle Image Velocimetry (PIV) to monitor the flow fields in the wave generation area. In their experiment, the water depth was 2.5 cm and stroke varied from 1.5 to 5.0 mm. At such a small scale, the free surface profiles of the generated waves were well predicted with linear theory.

Existing experimental studies are mostly limited to wave elevation histories. In contrast, observations of the flow field, as well as the nonlinear effects during wave generation are very scarce. Analytical descriptions of the velocity field in the source region have not been developed, perhaps due to the lack of experimental observations. As a result, the flow details in the source region are still not well understood.

To address the limitations of existing research, we performed a series of experiments at a scale roughly one order larger than Jamin et al. (2015). Our setup involved two independently movable bed segments, capable of moving up or down. Additionally, we derived the linear solutions for the velocity potential, from which we calculated the velocity field. The aims and objectives of this study include:

- To present PIV measurements for the flow field in the generation region, as well as the surface elevation histories for the wave propagation into an open sea;
- To derive and validate an analytical solution for the flow field based on potential flow theory and to investigate the range of applicability of these linear solutions;
- To explore the nonlinear behaviour during the wave generation and propagation;
- To investigate the similarities between the wave trains generated by vertical bed movements and real-world seismic tsunami events.

Through this study we target to achieve a better understanding of the wave trains generated by vertical bed movements. This paper is organized as follows: Section 2 describes the experimental devices, setup and cases; Section 3 describes an extension of the linear theory to retrieve the velocity potential and the computation of the velocity field. Results are presented and discussed in Section 4 and the paper finishes with conclusions in Section 5.

2. Experiment setup

2.1. Physical model

The experiments were conducted in the research wave tank at Swansea University. The tank is 30 m long, 1.2 m high and 0.8 m wide with glass sides. Two rectangular plexiglass boxes were mounted in the flume within a plexiglass carcass, which were 0.305 m long and covered the width of the tank. Fig. 1(a) shows the wave generating mechanism. Each box was driven independently by two actuators powered by an air compressor running at a fixed pressure. The boxes (segments) could move vertically up or down with a stroke of 0.05 m. The segments had the form of an inverted open rectangular box which allows water to move freely within the carcass but not into the water body above. All faces of the carcass were blocked except the left-hand side which was
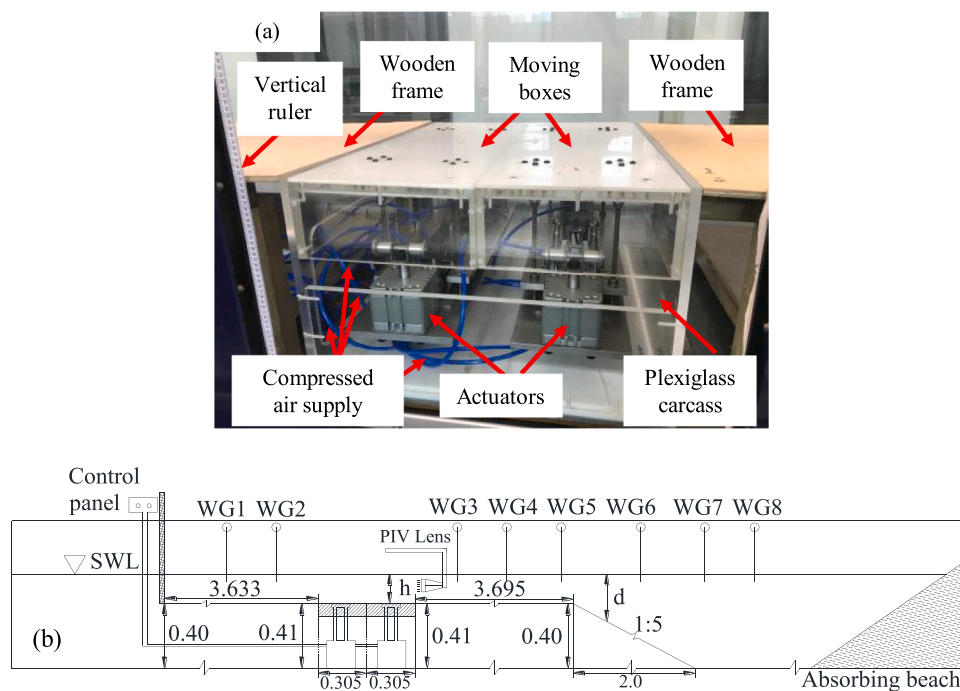
Fig. 1. (a) the vertically moving boxes as the wave generator; (b) the experimental setup and parameters (not drawn to scale but the dimensions are shown, unit: metre)

open for the access of compressed air supply. The segments' top faces were positioned at a height of 0.41 m above the base of the tank in their equilibrium position. A vertical ruler was located beside the left box for measuring the bed movement history.

The experimental setup is shown in Fig. 1(b). Our focus centred on the waves propagating to the right of the wave generator, with the seabed profile designed to reflect the bathymetry patterns spanning from the coastline to the expansive open ocean. Approximately horizontal wooden frames were connected to both sides of the carcass, with an elevation of 0.41 m at the edges of the carcass and 0.40 m at the ends. To the right of the carcass, the wooden frame was 3.695 m long, which simulated a continental shelf with a slight angle of $\sim 0.15°$, as the real-world continental shelf exhibits an average slope of $0.1°$ (Slatt, 2013). This frame was further connected to the tank base with a wooden slope of 1:5, representing a continental slope with an inclination of $\sim 11.31°$, as the real-world continental slope typically ranges from $1°$ to $10°$ (Pinet, 2019). The level bed beyond the wooden slope served as a representation of the deep ocean floor. To the left of the carcass, the wooden frame was 3.633 m long ending with a vertical wall. Thus, the region above the wooden framework was hydraulically insulated from the region below. As shown in Fig. 1(b), the water depth on the flat wooden frame is denoted by h, and the local water depth at a specific point in the experiment area is denoted by d. Eight wave gauges were installed in the tank, labelled WG1 to WG8. WG1&4 and WG2&3 were located symmetrically with respect to the common border of the two segments, with horizontal distances of 2.44 m and 0.54 m, respectively. WG5 to WG 8 were located to the right side of WG4, at distances of 3.94 m, 5.04 m, 6.34 m, 8.44 m from that common border, respectively. The purpose of setting WG1&2 was to check the symmetry of the generated wave and hence the symmetry of the movement of the two boxes, by comparing with the measurements at WG3&4. The area to the right of the boxes was divided into 3 regions according to the local water depth: region 1 (the left side of WG5) with the water depth of h; region 2 (WG5 to WG7) with an increasing water depth (d) on the slope; region 3 (beyond WG7) with a deeper constant water depth d equal to $0.41+h$.

A PIV system was set up to measure the flow field and bed movement, with the laser lens located 0.2 m from the right edge of the carcass.

A high-speed camera (SpeedSense 1040, 193 fps sustained at 4 MP resolution) was located to view transversely across the tank, in line with the common border of the two moving bed segments, to provide a direct view of the centre of the generation area. Seeding particles for the PIV were round polyamide beads with an average diameter of 50 μm and density of 1.03 g/cm^3. DynamicStudio (version 2015a) software was used for the image processing. Velocity vectors were obtained through the 'Adaptive PIV' process, in which the interrogation area lay in the range of 32×32 pixels to 64×64 pixels, and the particle detection limit was 5 pixels.

There were some important differences between the experimental set-up used by Hammack (1972) and the current one. Hammack (1972) used a servo-controlled platform installed at the bottom of one end of a tank (with the bottom walls of the moving bed segments exposed to the atmosphere), thereby forcing the generated waves to propagate in one direction only. In our experiment, the moving segments were submerged below the still water level, installed at the middle of the tank, and controlled by actuators instead of a constantly controlled servo. The waves generated in our experiment could propagate in both directions, and the leftward-propagating wave was reflected at the vertical wall. Due to the time delay, the reflected wave could easily be distinguished from the isolated pulse of the leading rightward propagating waves. Compared with Hammack (1972), our experiments included some new features:

- The flow field could be explored in detail with the PIV system, and the generated wave could propagate both sides to allow the study of symmetry;
- The seabed movement included both unimodal and bimodal types, covering a wider range of types of bed movements;
- The nearly horizontal wooden frame (region 1), shelving slope (region 2) and the area with increased water depth (region 3) represented the real-world bathymetry, rather than the frequently used flatbed. This allowed the study of the wave propagation from the coastline to the expansive open ocean.

There were some known limitations of the experimental set-up, as

listed below:

- The two boxes were controlled independently and differ in their hydraulic connectivity, resulting in slightly different movements. Based on experiment recordings, the boxes' movements aligned well with half-sine functions (see Section 2.3 and Eq. (3)). The influence of less-than-ideal seabed movement was insignificant in most cases.
- The experiments were considered to be a 2D case in which the generated waves propagate parallel to the flume. As the moving bed matched the flume width, any 3D effects were mitigated in our experiment.
- According to Das and Melan (2023), compressibility is insignificant unless the water depth is sufficiently deep or the bottom movement is sufficiently rapid, and the error is up to 0.55 % at 4000 m depth. Given the small scale, shallow water depths and rigid moving bottom adopted in our experiment, the influences of water compressibility and bottom elasticity have been ignored.

2.2. Case settings

We investigated eight movement modes which were categorized into two types as listed in Table 1: unimodal mode (UM, modes 1 to 6) and bimodal mode (BM, modes 7 and 8). UM cases involved the movement of a single moving segment (modes 1 and 2 with the right segment, UM-R; modes 5 and 6 with the left segment, UM-L) or both segments moving together in the same direction (modes 3 and 4, UM-D). BM cases involved two segments moving in opposite directions simultaneously. The generated wave train was also defined by whether the first extremum recorded at WG3 was a crest (crest-leading, CL), or a trough (trough-leading, TL). Experiments were conducted for four water depths (h = 0.1, 0.2, 0.3 and 0.4 m), making a total of 32 cases.

Fig. 2 shows the key parameters used in the analysis. At a fixed wave gauge, the first extremum (leading crest or leading trough) and the subsequent second extremum were denoted by η_1 and η_2, respectively, and their corresponding appearance times were denoted by $t_{\eta1}$ and $t_{\eta2}$. The height of the first full wave (crest-trough or trough-crest) was denoted by η_0, with $\eta_0 = |\eta_1| + |\eta_2|$. The arrival time t_a was defined as the moment when the rising (or falling) water level first exceeded $0.05\eta_1$. The wave period (T) was defined by the duration from t_a to the time when the elevation crossed the still water level the second time, which was the sum of the durations of the first and second half periods ($T_{\eta1}$ and $T_{\eta2}$, respectively). The average speed $\bar{c}$ was calculated as the ratio of the
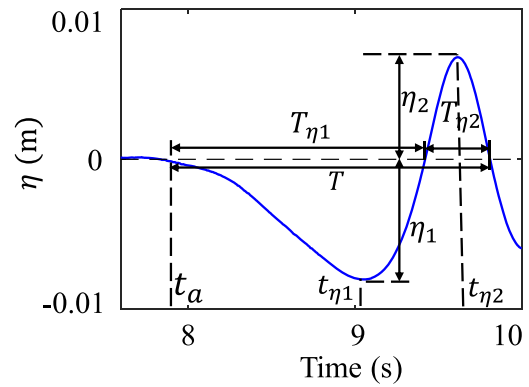

Fig. 2. The definition of the wave parameters.

distance between wave gauges and the difference in arrival times. The $\bar{c}$ at each wave gauge was estimated by interpolation or extrapolation. The wavelength (L) was calculated as the product of $\bar{c}$ and T.

2.3. Bed movement

The bed movements were recorded with the high-speed camera and digitized into time series $\zeta(t)$, allowing the idealization of the bed movement using half-sine functions (Eq. (3)). Taking Test 6 (UM-L-TL, h = 0.1 m) and Test 15 (BM-TL, h = 0.2 m) as examples, Fig. 3 shows snapshots of the bed movement for these two cases, and the recorded bed movements are presented in Fig. 4, demonstrate the good approximation with half-sine functions.
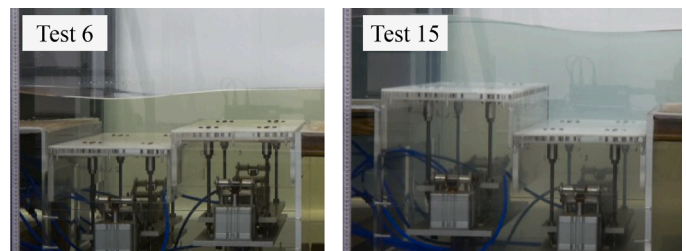

Fig. 3. The snapshots of the moving bed segments in Tests 6 and 15.

Table 1
The bed movement modes and all test definitions (the parameters α and δ are introduced in Section 2.3).

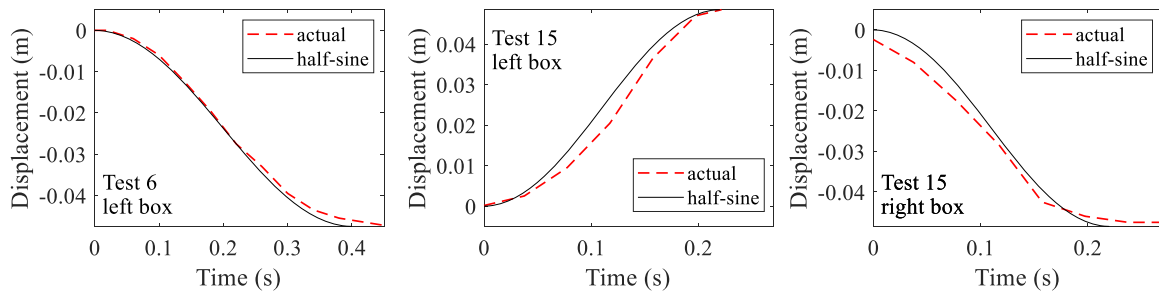| Mode		Left box	Right box	Sketch	h = 0.1 m (α = 0.5)	h = 0.2 m (α = 0.25)	h = 0.3 m (α = 0.167)	h = 0.4 m (α = 0.125)
1	UM-R-CL	still	↑		Test 1 (δ = 1.525)	Test 9 (δ = 0.763)	Test 17 (δ = 0.508)	Test 25 (δ = 0.381)
2	UM-R-TL	still	↓		Test 2 (δ = 1.525)	Test 10 (δ = 0.763)	Test 18 (δ = 0.508)	Test 26 (δ = 0.381)
3	UM-D-CL	↑	↑		Test 3 (δ = 3.050)	Test 11 (δ = 1.525)	Test 19 (δ = 1.016)	Test 27 (δ = 0.763)
4	UM-D-TL	↓	↓		Test 4 (δ = 3.050)	Test 12 (δ = 1.525)	Test 20 (δ = 1.016)	Test 28 (δ = 0.763)
5	UM-L-CL	↑	still		Test 5 (δ = 1.525)	Test 13 (δ = 0.763)	Test 21 (δ = 0.508)	Test 29 (δ = 0.381)
6	UM-L-TL	↓	still		Test 6 (δ = 1.525)	Test 14 (δ = 0.763)	Test 22 (δ = 0.508)	Test 30 (δ = 0.381)
7	BM-TL	↑	↓		Test 7 (δ = 3.050)	Test 15 (δ = 1.525)	Test 23 (δ = 1.016)	Test 31 (δ = 0.763)
8	BM-CL	↓	↑		Test 8 (δ = 3.050)	Test 16 (δ = 1.525)	Test 24 (δ = 1.016)	Test 32 (δ = 0.763)

Fig. 4. The recorded bed movement time series and corresponding half-sine curves of Tests 6 and 15.

Following Hammack (1972) the characteristics of the bed movement are described with three parameters: the maximum movement distance ζ_0, the movement duration T_0 (the time that the bed reached ζ_0) and characteristic time t_c (the time that the bed reached 2/3 of ζ_0). The properties of the moving bed were described by two parameters: disturbance-amplitude scale (ζ_0/h, denoted by α) and the disturbance-size scale (b/h, denoted by δ), in which $2b$ is the width of the moving bed segment. Fig. 5 showed ζ_0 and average bed movement speed (ζ_0/T_0) for all cases. ζ_0 lay in the range of [0.035 m, 0.053 m] and the movement speed lay in the range of [0.09 m/s, 0.29 m/s]. The values of ζ_0 were clustered around 0.05 m while those of ζ_0/T_0 showed a little more scatter. There was no clear behavioural trend for ζ_0 and ζ_0/T_0 with water depth. Generally, in the bimodal cases the bed segments travel over a slightly greater distance and at a faster speed than in the unimodal cases, and the segments tend to move slightly faster when moving downward than when moving upward.

Hammack (1972) proposed a classification of bed movement based on the 'time-size parameter ($t_c\sqrt{gh}/b$)' and 'disturbance-amplitude scale (α)':

(1) impulsive movement, for which $t_c\sqrt{gh}/b \ll 1$, and the generated wave does not have enough time to escape from the moving area during the movement, and linear theory is only applicable for $\alpha \ll 1$;

(2) creeping movement, for which $t_c\sqrt{gh}/b \gg 1$, and the generated wave can propagate away while the seabed is still moving, and linear theory is applicable regardless of the value of α;

(3) intermediate movement, in which the movement characteristics lie between impulsive and creeping movements.

The variation in experimental parameters resulted in the ranges for α and δ of 0.125 to 0.5, and 0.38 to 3.05, respectively. Fig. 6 presents the
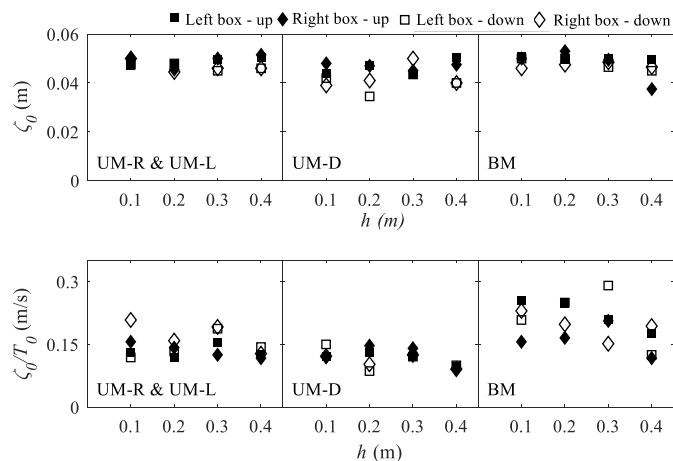

Fig. 5. The movement distances (ζ_0, top panel) and average movement speed (ζ_0/T_0, bottom panel) of the segments.
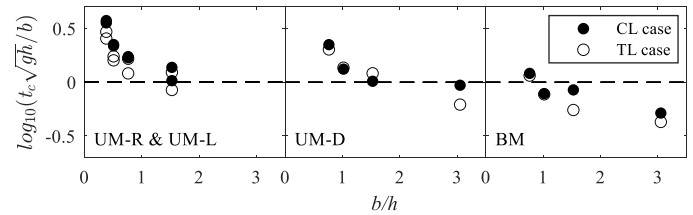

Fig. 6. The bed movement parameter $t_c\sqrt{gh}/b$ for different b/h and bed movement modes.

values of $t_c\sqrt{gh}/b$ against b/h for all 32 tests, which vary between 0.69 and 1.70, showing that all our tests fell into the 'intermediate' movement type. Parameters of the seabed earthquakes of the 2004 Boxing Day tsunami and 2011 Tohoku tsunami were calculated for the comparison with our experiments. According to Wang and Liu, (2006), the Boxing Day tsunami resembled a two-segment movement with a total width of 150 ~ 200 km, local water depth of ~ 5 km, stroke of ~ 3 m and moving time of ~ 600 s. This resulted in values of α around 0.0006, δ in the range 15 to 20 and $t_c\sqrt{gh}/b$ between 0.89 and 1.18. For the Tohoku tsunami, the width of the uplifted fault was about 200 km, water depth ranged from approximately 1000 m to 1600 m (extracted from the water depth of two gauges close to the centre of the fault, TM1 and TM2), the stroke was ~ 3 m and movement duration was ~ 240 s (Maeda et al., 2011; Sato et al. 2011; Satake et al., 2013). Thus, the estimated α was between 0.0019 and 0.003, δ ranged from 62.5 to 100 and $t_c\sqrt{gh}/b$ was between 0.16 and 0.20.

It is evident that the bed movements associated with these two well-known tsunami events fell under the 'intermediate' type, which is similar to our experiment. However, their values of α were of the order of 10^{-3} and δ was between the orders of 10 and 10^2, exhibiting large differences with our experimental settings with shallower water depths and smaller sizes of the faults. Specifically, our experiment is of relevance to earthquakes occurring in very shallow coastal shelves and potentially to shallow seas where drilling, extraction and pumping of saline aquifers compromised the integrity of the residual rock structure which might lead to the collapse of the overbearing strata.

2.4. Reproducibility and symmetry

Each test in Table 1 was repeated three times, and the wave elevation histories for the three repetitions at each gauge were synchronized, displaying satisfactory agreement between the repetitions. For example, Fig. 7 compares the water elevation histories at all 8 wave gauges in Test 11 (UM-D-TL, $h = 0.2$ m). It is evident that the three curves overlap almost perfectly. The same pattern appears in all 32 cases, demonstrating the high reproducibility of our experiment. The averaged wave elevation histories, derived from the three repetitions, were calculated to provide a quantitative analysis of the level of agreement amongst the repetitions. The amplitudes of first extrema (η_1) and the 'rising durations' for η_1 (i.e., $t_{\eta 1} - t_a$) of each test were extracted. The mean values
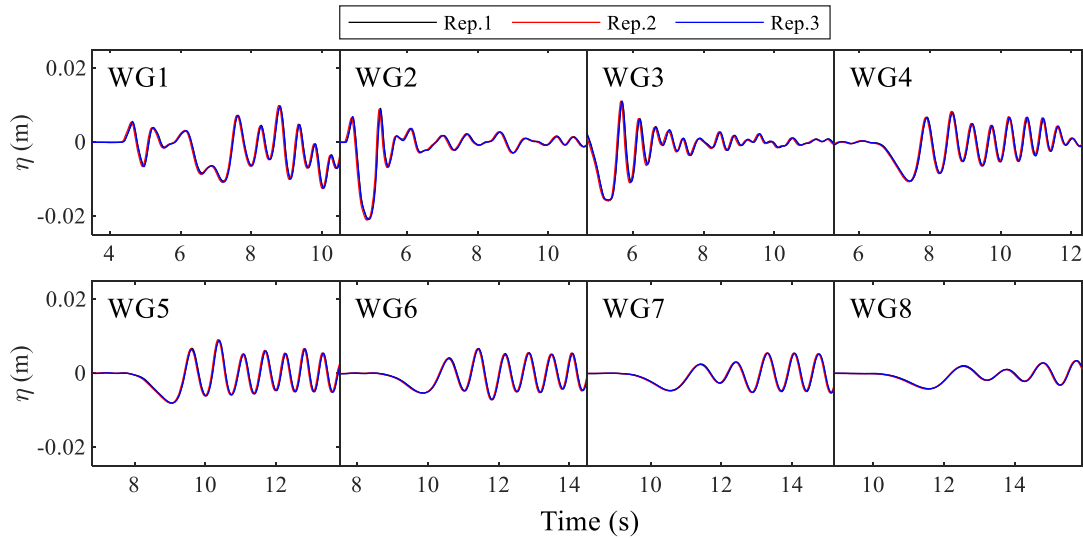
Fig. 7. The water elevation histories at all 8 wave gauges for the three repetitions for Test 11.

and standard deviations of these two parameters were computed to determine their relative standard errors (RSE), whose values at WG3 are presented in Table 2. It can be seen that tests with $h = 0.4$ m show higher errors in η_1. This is because the amplitudes of the generated waves were much smaller for this water depth, and a low discrepancy in absolute value leads to a larger RSE. However, for most tests the errors in η_1 were less than 5 % and the errors in $(t_{\eta1} - t_a)$ were less than 3 %, indicating a high level of reproducibility. The averaged wave elevation histories were used for the following analysis.

An approximately symmetric behaviour was evident in our experiment. Specifically, symmetric movement modes (e.g., UM-L and UM-R at the same water depth, or UM-D) were expected to produce identical wave elevation histories for symmetrically located wave gauges (WG1 versus WG4, WG2 versus WG3). For example, Fig. 8(a) compares the wave elevation histories at WG3 in Test 9 (UM-R) with that at WG2 in Test 13 (UM-L), and Fig. 8(b) compares those at WG2 and WG3 in Test 11(UM-D). Each curve in Fig. 8 exhibits two notable crests. The first crests occurred between $t = 4$ to 6 s (marked by the black dashed circles), describing the initial crests generated above the moving bed segments. Agreement was found between the red and blue curves on the arrival times (t_a), peak times $(t_{\eta1})$ and wave amplitudes (η_1) of the first crests. The second crests occurred between $t = 8$ to 12 s (marked by the green dashed circles), describing the wave crests generated by the reflection of the left-travelling initial crests by the vertical wall. While there is agreement in the amplitude of the second crest, there is a discrepancy in arrival times at WG3 (blue curves) and WG2 (red curves) because the reflected crests travelled a shorter distance to reach WG2. It is noted that left-hand and right-hand bed segments exhibited very small differences; attributed to variations in actuator performance and the differences in
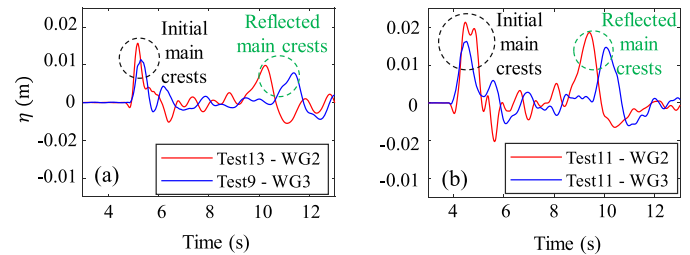

Fig. 8. (a) wave elevation histories of WG2 in Test 13 and WG3 in Test 9; (b) wave elevation histories of WG2 and WG3 in Test 11.

hydraulic connectivity. In conclusion, the bed movement mechanism showed symmetric behaviour to a reasonable degree, and the experiments were highly reproducible.

3. Linear solution for the generated wave train

Analytical solutions for the waves generated by the vertical displacements can be derived based on linear wave theory. For the governing equations and boundary conditions, the reader is referred to Hammack (1972). The solutions for the water-air interface and velocity potential are given in Eqs. (1) and (2), in Fourier- and Laplace- transformed form:

$$\widetilde{\overline{\eta}}(k,s) = \frac{s^2 \widetilde{\overline{\zeta}}(k,s)}{(s^2 + \omega^2)\cosh kh} \tag{1}$$

Table 2
The relative standard errors of η_1 and $(t_{\eta1} - t_a)$ for each test at WG3 (Unit: %).

Mode	Relative standard error of η_1				Relative standard error of $(t_{\eta1} - t_a)$			
	$h = 0.1$ m	$h = 0.2$ m	$h = 0.3$ m	$h = 0.4$ m	$h = 0.1$ m	$h = 0.2$ m	$h = 0.3$ m	$h = 0.4$ m
1	1.775	0.230	0.087	3.519	1.230	0.690	0.868	0.452
2	0.863	1.003	1.371	2.713	0.516	0.522	12.228	0.380
3	0.782	4.148	3.034	13.575	0.043	1.304	2.667	0.682
4	0.932	2.860	3.478	4.574	0.381	1.585	1.332	0.598
5	0.309	0.075	2.078	15.173	0.711	0.859	1.918	0.727
6	0.765	0.609	1.833	5.165	4.225	1.118	0.517	0.618
7	0.919	5.559	1.872	5.126	0.928	0.580	1.400	0.247
8	4.106	5.381	2.026	18.894	5.475	3.664	0.740	0.573
Average	1.306	2.483	1.972	8.592	1.689	1.290	2.709	0.535

$$\widetilde{\bar{\phi}}(k, y, s) = \frac{-gs\widetilde{\bar{\zeta}}(k,s)}{(s^2 + \omega^2)\cosh kh}\left[\cosh ky - \frac{s^2}{gk}\sinh ky\right] \quad (2)$$

The idealized half-sine function for the bed movement $\zeta(x, t)$ is given by Eq. (3). Applying a Fourier- Laplace transform to Eq. (3) yields Eq. (4):

$$\zeta(x,t) = \zeta_0\left[\frac{1}{2}(1-\cos\kappa t)\mathscr{H}(T_0 - t) + \mathscr{H}(t - T_0)\right]\mathscr{H}(b^2 - x^2) \quad (3)$$

$$\widetilde{\bar{\zeta}}(k,s) = \zeta_0\frac{\sin kb}{k}\left[(1 + e^{-sT_0})\frac{\kappa^2}{s(s^2 + \kappa^2)}\right] \quad (4)$$

Substituting Eq. (4) into Eq. (1) and applying the inverse transform, the solutions for the surface displacement generated by unimodal and bimodal bed movements may be found and are given in Eq. (5) and Eq. (6), respectively (see Hammack (1972); Shen et al. (2022)):

$$\eta(x,t) = \frac{\zeta_0}{\pi}\int_0^\infty \frac{k^2}{k^2 + \omega^2}\frac{\cos kx}{k\cosh kh}\sin kb\{\cos\omega t - \cos\kappa t$$
$$+ \mathscr{H}(t - T_0) * [\cos\omega(t - T_0) + \cos\kappa t]\}dk \quad (5)$$

$$\eta(x,t) = \frac{\zeta_0}{4\pi}\int_{-\infty}^\infty \frac{k^2}{k^2 + \omega^2}\frac{2\sin kx + \sin(2kb_2 - kx) - \sin(2kb_1 + kx)}{k\cosh kh}$$

$$\{\cos\omega t - \cos\kappa t + \mathscr{H}(t - T_0) * [\cos\omega(t - T_0) + \cos\kappa t]\}dk \quad (6)$$

The flow field cannot be directly calculated from the analytical solutions of the surface displacement, and solutions for the velocity potential are required. By substituting Eq. (4) into Eq. (2) and applying the inverse transforms, the solutions for unimodal and bimodal movements were formulated, as shown in Eq. (7) and Eq. (8), respectively:

$$\phi(x, y, t) = \frac{g\zeta_0}{2\pi}\int_{-\infty}^\infty \frac{\cos kx \sin kb}{k\cosh kh}\frac{1}{\kappa^2 - \omega^2}$$
$$\left[\left(\kappa\cosh ky + \frac{\kappa^3}{gk}\sinh ky\right)(\sin\kappa t - \mathscr{H}(t - T_0)*\sin\kappa t)\right.$$
$$\left. - \left(\frac{\kappa^2}{\omega}\cosh ky + \frac{\omega\kappa^2}{gk}\sinh ky\right)(\sin\omega t + \mathscr{H}(t - T_0)*\sin\omega(t - T_0))\right]dk \quad (7)$$

$$\phi(x, y, t) = \frac{g\zeta_0}{2\pi}\int_{-\infty}^\infty \frac{-\sin kb_1*\cos k(x + b_1) + \sin kb_2*\cos k(x - b_2)}{k\cosh kh}\frac{1}{\kappa^2 - \omega^2}$$
$$\left[\left(\kappa\cosh ky + \frac{\kappa^3}{gk}\sinh ky\right)(\sin\kappa t - \mathscr{H}(t - T_0) * \sin\kappa t)\right.$$
$$\left. - \left(\frac{\kappa^2}{\omega}\cosh ky + \frac{\omega\kappa^2}{gk}\sinh ky\right)(\sin\omega t + \mathscr{H}(t - T_0) * \sin\omega(t - T_0))\right]dk \quad (8)$$

It should be noted that these analytical solutions are valid from the source region up to WG5, (region 1), as they are not applicable in regions with significantly varying still water depth. Eqs. (7) and (8) were evaluated on a grid of points in the x-y domain using numerical integration. The $y = 0$ level was taken to be the still water level and $x = 0$ was at the juncture of the two moveable seabed segments. Horizontal and vertical velocity components at each point were computed from the derivatives of the velocity potential using first-order finite-difference approximations. By substituting the movement amplitude (ζ_0) and movement duration (T_0) of each test into Eqs.(5) to (8), the results corresponding to our experiments can be found. Comparisons between the theory and observations are presented in Section 4.2.

4. Results

In this section we begin by presenting the results for both unimodal

and bimodal bed movements, based on the scalar and vector maps along with the free surface profiles recorded by PIV system. Secondly, we analyse the wave propagation characteristics. Thirdly, we compare the experimental measurements with the analytical results of each test, and examine the applicability of the linear theory. Finally, a brief discussion of non-linear aspects of the wave behaviour is provided.

4.1. Experiment of wave generation and propagation

4.1.1. Wave generation of unimodal (UM) cases

Unimodal cases behaved consistently for cases with $\alpha \leq 0.25$. When $\alpha = 0.5$, wave behaviour was significantly influenced by the high non-linearity, which is discussed in Section 4.3.1. To describe the general wave generation process for unimodal cases with $\alpha \leq 0.25$, we took Tests 9 and 10 as examples (UM-R-CL and UM-R-TL cases with $\alpha = 0.25$). PIV snapshots of the wave generation in these two cases is presented in Fig. 9. The bed movement induced a laminar-like velocity field in the water above. Initially, the velocity was distributed radially, with the contour resembling the upper half of an ellipse (see the top row of Fig. 9). The rising bed pushed the water to the top-, left- and right-hand sides, while the falling bed induced a movement in the opposite sense. The free surface was shaped as a concave (CL cases) or convex (TL cases) bulge, with the horizontal length larger than that of the moving bed segment. This is a feature of the 'intermediate' bed movement type, as the wave begins to propagate before the bed movement ceases.

The vertical movement of free surfaces persisted for a short duration after the bed movement stopped, until the water at the free surface lost momentum (see the light-blue areas on the convex or concave profiles in the middle row of Fig. 9). Under gravitational adjustment, this 'quiescent area' moved vertically downwards, as the vertical velocity above the bed reversed. Above the moving bed, the water flow at the centre showed lower speed than that at the edges. The bulge and the 'half ellipse' velocity contour began to separate, forming the initial extrema of the wave train (η_1), and a mushroom-like velocity contour map (see the middle row of Fig. 9). No vortex was evident above the displaced bed segment.

The water surface subsequently moved back towards the still water level, overshooting due to inertia, to create a secondary convex (TL cases) or concave (CL cases) surface above the fault. Under gravity, the new bulge split, forming the secondary extrema of the generated wave train (η_2). At this time, the near-bed velocities became very small while velocities were enhanced near the free surface (see the bottom row of Fig. 9). The consequent cycle of recovery and breaking of equilibrium generated the following diminishing wave train. Vortices were observed at the sharp corners of the faults (see the bottom row of Fig. 9). The vortex at the right corner of the fault in Test 10 was more intense, due to some leakage from beneath the wooden frame. Comparing the left and right panels of Fig. 9, the shape of the speed contours and isotachs of the TL and CL cases were highly similar, indicating a linear dynamical response.

4.1.2. Wave generation of bimodal (BM) cases

Bimodal cases also behaved differently depending on whether $\alpha \leq 0.25$ or $\alpha = 0.5$ due to the non-linearity of the flow that developed in shallow water. To discuss the general process for bimodal cases with $\alpha \leq 0.25$, we take Test 16 ($h = 0.2$ m and $\alpha = 0.25$) as an example. Fig. 10 presents the PIV snapshots for the wave generation in this case. A bimodal bed movement involved simultaneous upward and downward bed shifts, creating a complex flow field. Bimodal bed movements generated high-velocity areas with different flow directions on both moving segments, with the highest velocities appearing close to the common border of the two boxes. A curved flow from the rising to the falling segment was observed (Fig. 10, $t = 0.10$ s). Above this common border, the water surface was relatively undisturbed, because the two bed segments led to a zero net volume change in the water column. At about $t = 0.20$ s, the free surface above the faults exhibited a sinusoidal
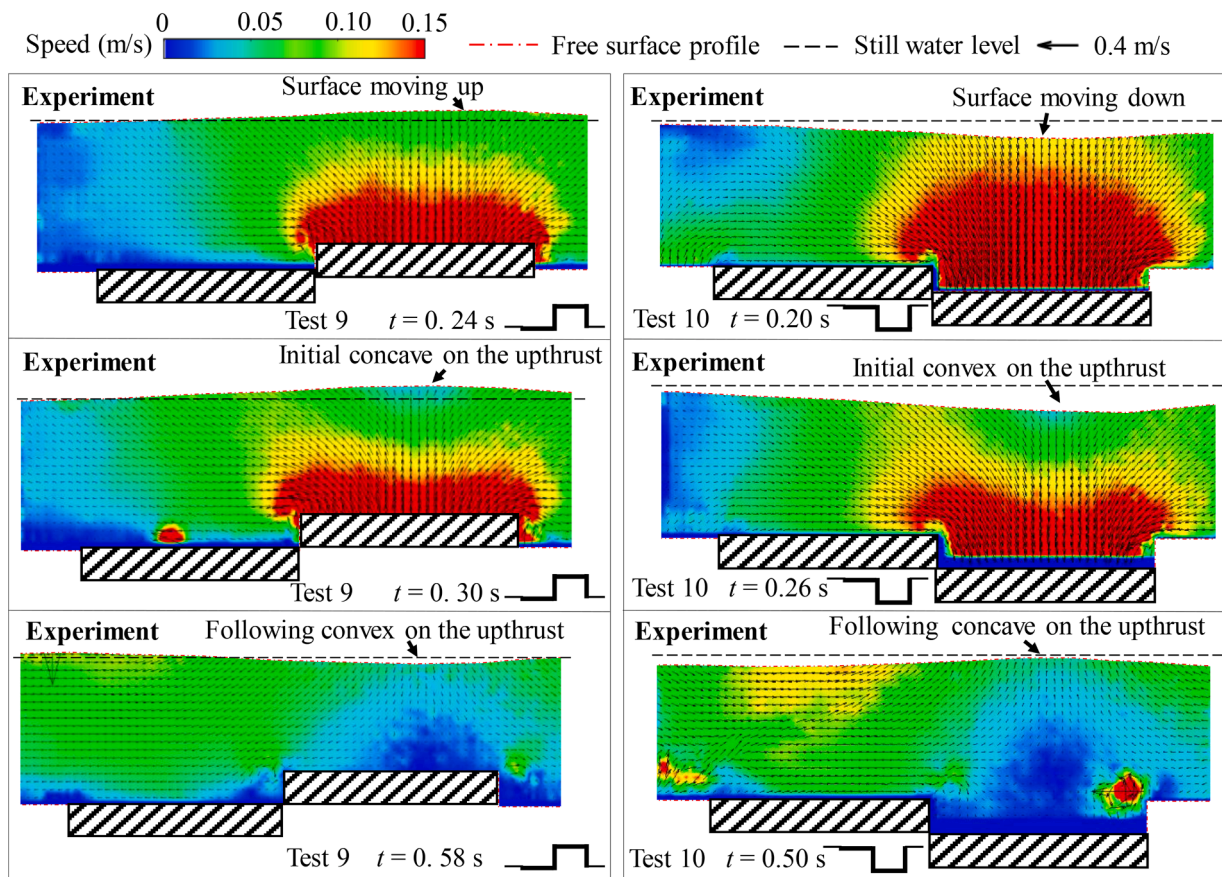
Fig. 9. Free surface profiles, vector maps and isotachs of the velocity field derived from PIV measurements for Tests 9 (h = 0.2m, left column) and 10 (h = 0.2m, right column) for the generation of η_1 and η_2.
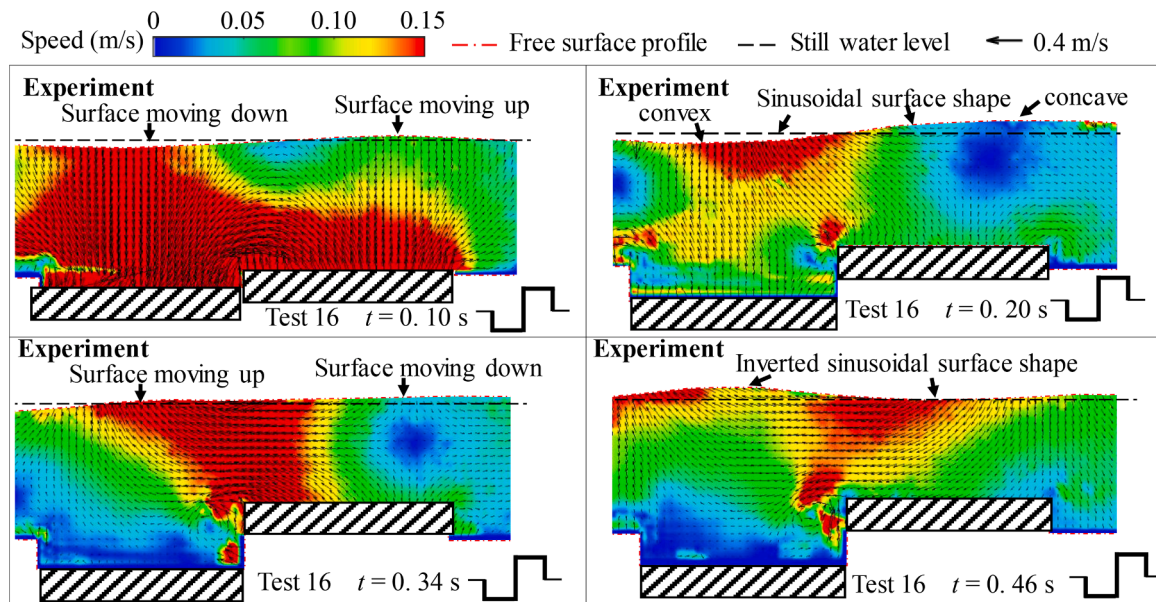

Fig. 10. Free surface profiles, vector maps and isotachs of Test 16 derived from PIV measurements during a bimodal bed movement, (BM-CL, h = 0.2 m).

shape, subsequently splitting to generate wave trains. After the bed movement stopped, the distorted surface adjusted towards its equilibrium position (Fig. 10, t = 0.34 s) and overshot the equilibrium, thereby producing an inverted sinusoidal-like free surface profile. The subsequent oscillations about equilibrium inducing a wave train of diminishing amplitude (Fig. 10, t = 0.46 s). For the right-travelling wave train, both the two leading extrema (η_1 and η_2) were significant and of a similar magnitude, (whose main contributions were the initial concave and convex at 0.20 s, respectively), in contrast with the unimodal cases.
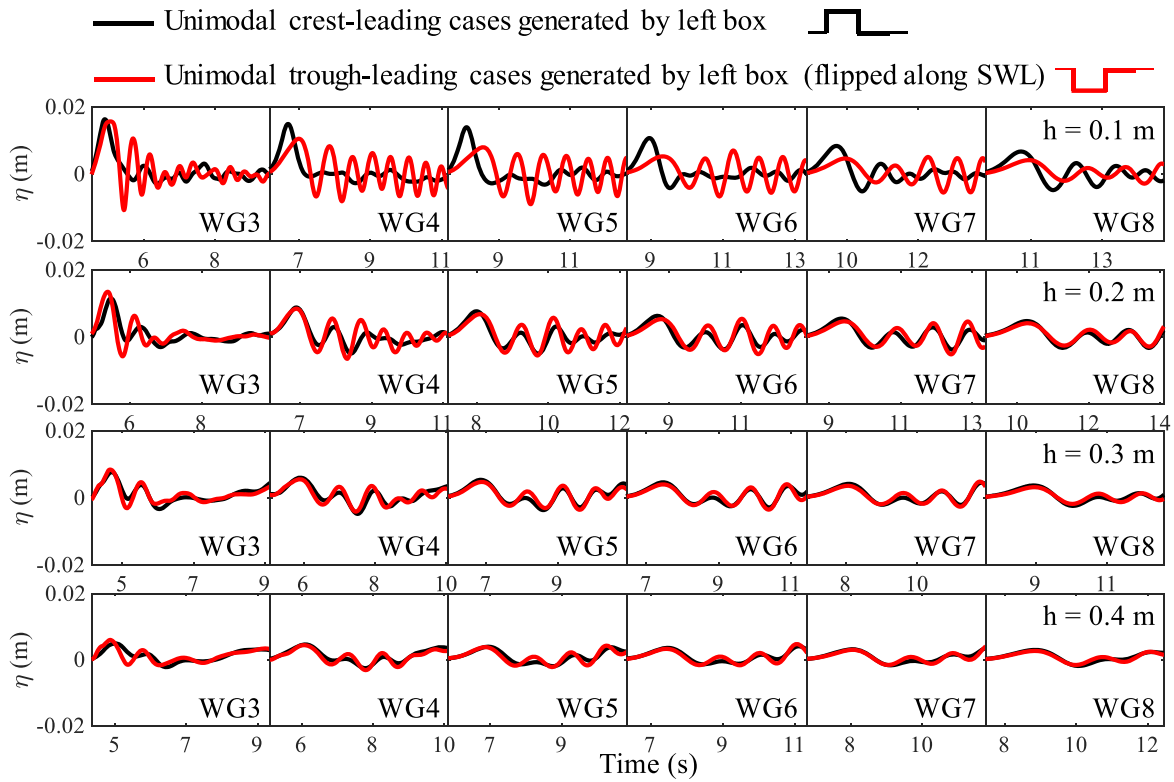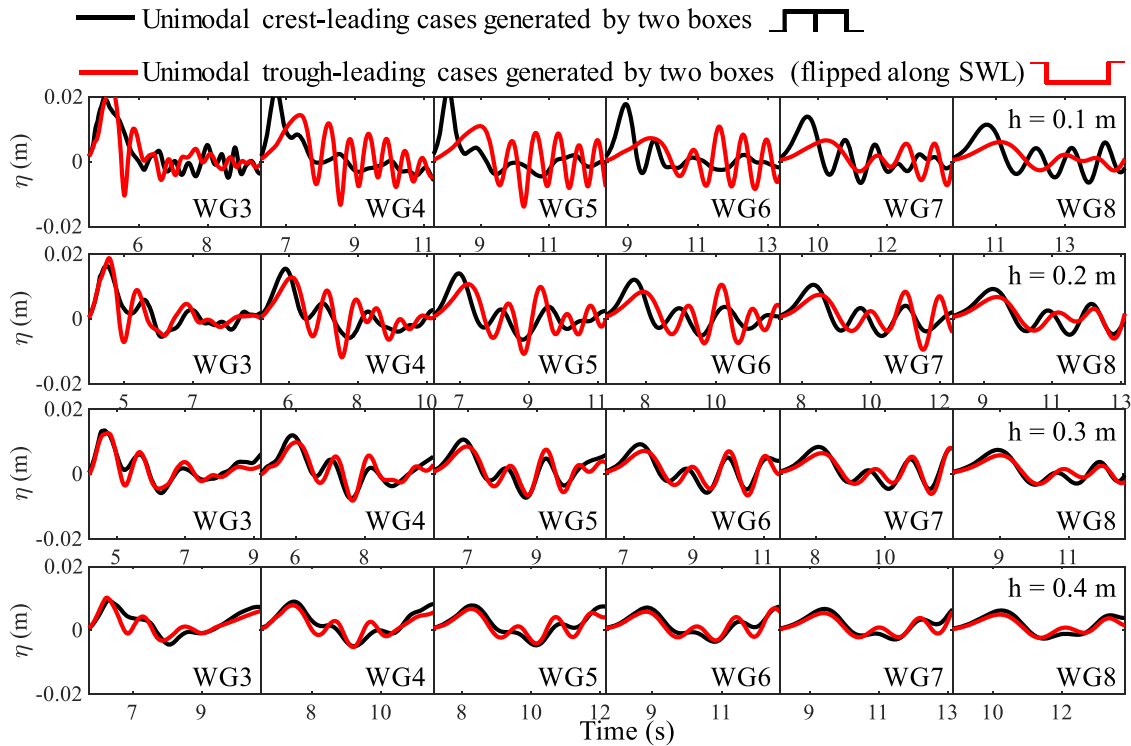
Fig. 11. The water elevation histories of WG3 to WG8 of all UM-L tests (the trough-leading cases are mirrored along the still water level)
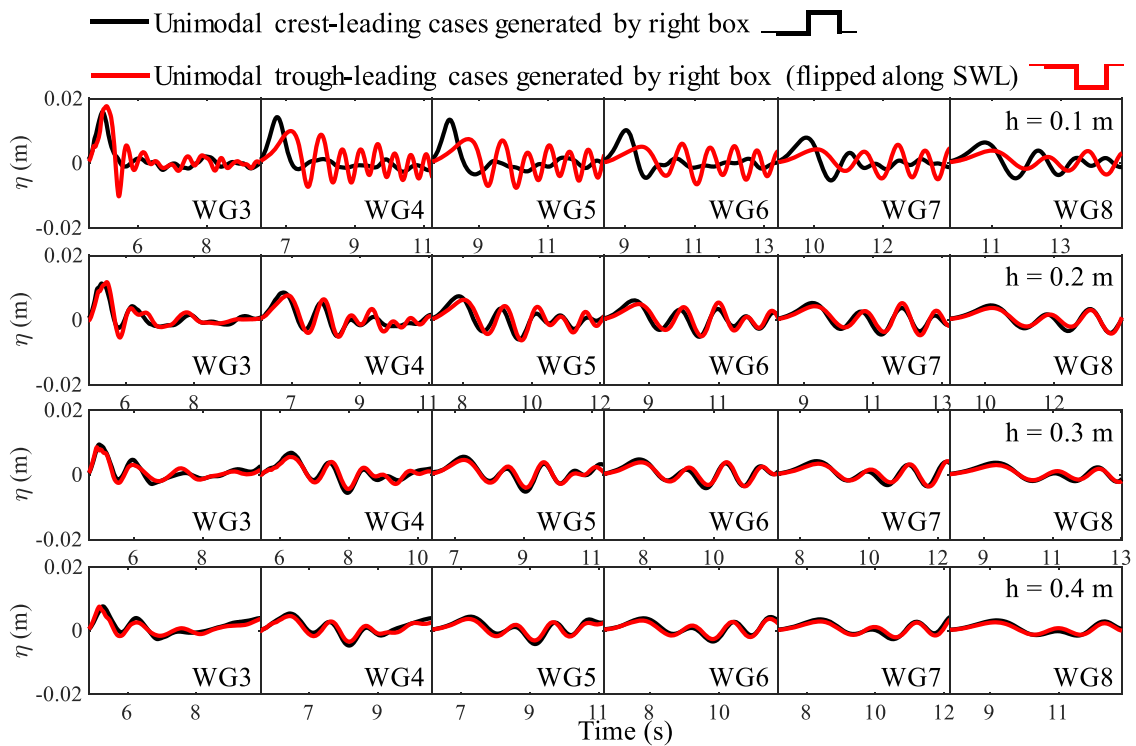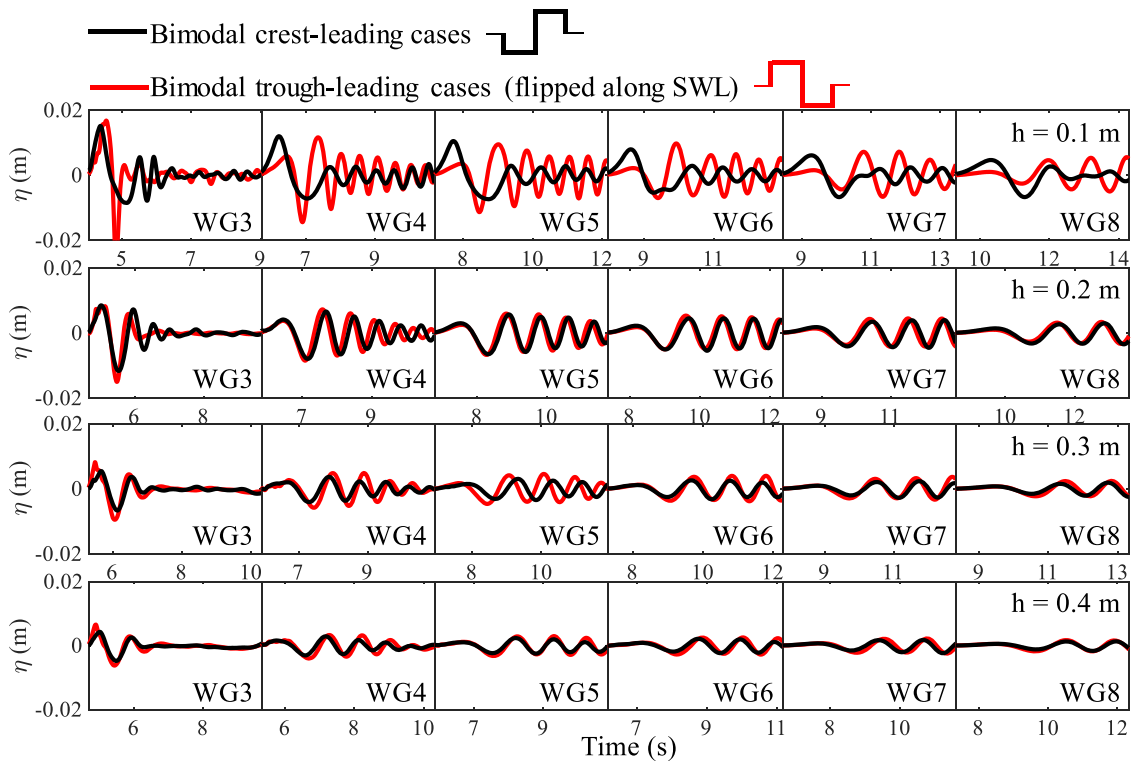

Fig. 12. The water elevation histories of WG3 to WG8 of all UM-R tests (the trough-leading cases are mirrored along the still water level)

4.1.3. Characteristics of wave propagation

Figs. 11 to 14 show the experimental observations of surface elevations at wave gauges WG3 to WG8 for all cases. The plots for trough-leading cases have been reflected about the still water level for ease of

comparison. The unimodal cases are characterized by a significant initial extremum (η_1) followed by a less significant extremum (η_2), while η_1 and η_2 are of very similar magnitude for bimodal cases. According to linear theory, (Eqs. (5) and (6)), when δ, α, T_0 are fixed, waves generated

Fig. 13. The water elevation histories of WG3 to WG8 of all UM-D tests (the trough-leading cases are mirrored along the still water level)

Fig. 14. The water elevation histories of WG3 to WG8 of all BM tests (the trough-leading cases are mirrored along the still water level)

by bed movements with strokes of ζ_0 and $-\zeta_0$ should be the mirror image of each other about the still water level. This linear behaviour is observed in cases with $\alpha \leq 0.25$ ($h \geq 0.2$ m). As shown in Figs. 11 to 14, the mirror images of the wave histories of trough-leading cases overlap well with the wave histories of their crest-leading counterparts. For

lower values of α and δ, this agreement becomes closer, indicating greater linearity. However, for bed movements with $\alpha = 0.5$ ($h = 0.1$ m), there is a strongly asymmetric response in the crest-leading and trough-leading cases. Braddock et al. (1973) concluded that the generated wave trains might eventually transfer into a solitary wave followed by a

periodic wave train, and this phenomenon was observed in our experiment. The crest-leading wave train behaves like a solitary wave followed by an insignificant trough and a train of smaller waves. In the trough-leading case the leading trough decays significantly and the wave train evolves towards a sequence of regular-like waves of diminishing amplitudes. One notable feature in this case is the high and steep peak following the leading trough, (see Fig. 14 left-hand panel of the top row).

Figs. 15 to 18 plot six normalized parameters: $|\eta_1/\zeta_0|$; $|\eta_2/\zeta_0|$; $\overline{c_0}/\sqrt{gd}$; $T_{\eta1}/T_0$; $T_{\eta2}/T_0$ and L/b. These measure the amplitude of the first extremum, the amplitude of the second extremum, the average celerity, the half-period of the first and second waves; and the wavelength of the leading wave, respectively. The ratio of the local water depth (d) and wavelength (L) are shown in Fig. 19. Some key features can be observed from them:

- Near the wave generation area, the first extrema were much larger than the second extrema for unimodal cases while the two extrema were of similar magnitude in the bimodal cases (see Fig. 15);
- For a fixed water depth, the bimodal cases generated slightly lower first extrema than those of the unimodal cases with a single moving segment, due to the non-linearity from the wave generation and wave-wave interactions;
- Comparing the UM-L/UM-R cases ($b = 0.1525$ m) and UM-D cases ($b = 0.305$ m), the amplitudes of the first extrema increased with the size of the moving bed (Fig. 15), but this phenomenon was less obvious at a larger water depth. The amplitudes of the second extrema (Fig. 15) and the half periods of the leading wave cycles (Fig. 16) were less sensitive to the size of the moving bed;
- For a fixed bed movement mode, a smaller water depth led to larger amplitudes of the first two extrema. This is because a shallower water depth weakened the inertial resistance from the water above the moving bed segment and led to a larger disturbance-amplitude scale (α);
- The waves exhibited longer first half periods ($T_{\eta1}$) than the following second half periods($T_{\eta2}$), indicating asymmetry (see Fig. 16);
- For each test, the first extremum travelled with a speed remaining within the range of 80 % to 120 % of the linear shallow water wave celerity, even in the region 3 with increased water depths (see Fig. 17). According to the Airy wave criteria for categorising surface waves, all the waves in the experiment were intermediate waves near the generation region and transformed towards shallow water waves with the propagation (see Fig. 19).
- Most exceptions to the above occurred for cases with $h = 0.1$ m ($\alpha = 0.5$), because of the stronger non-linear effects, which will be discussed in Section 4.3;

Wave decay was observed, with the reduction of wave amplitude (see Fig. 15) and increase of wave periods and wavelengths (see Figs. 16 and 18), the key characteristics of the wave decay are summarized as follows:

- The most significant wave decay occurred near the wave generation area (WG3 to WG4), while the first extrema (η_1) decayed more substantially than the second extrema (η_2) and the following wave trains.
- The increasing water depth in region 2 led to significant reduction of η_1, being similar to the reverse process of wave shoaling.
- η_2 remained much more stable than η_1, and the wave periods and wavelengths increased at stable rates beyond WG4.
- A higher initial water depth (h) led to lower decaying rates for the leading extrema in all three regions (see Fig. 15).

Due to the wave decay, long-distance propagation may lead to the disappearance of the leading half period and an increase the importance of the following regular-like wave trains. As shown in Fig. 15, η_1 reduced to the same magnitude as η_2 at the end of region 1, and became lower than η_2 (or even close to zero) at the end of region 3. According to Figs. 11 to 14, the amplitudes of the regular-like wave train may be higher than the extrema of the leading cycles (η_1 and η_2). These phenomena have been observed in real-world seismic tsunami events, for example:

- The initial wave was not always the largest in the group for the 2004 Boxing Day tsunami, and the leading crest eventually disappeared far from the fault (Merrifield et al., 2005).
- Regular wave trains were observed over an extended duration for the 2011 Tohoku tsunami, and wave trains continued to arrive at the US west coast for more than 48 h (Allan et al., 2012).

4.2. Comparison against analytical solutions

4.2.1. Wave generation

Linear theory provided generally good predictions of the cases with $\alpha \leq 0.25$, although some discrepancies arose for cases with $\alpha = 0.25$. Fig. 20 shows examples from Tests 9, 15 and 28 at specific time instants, representing UM-R, UM-D and BM cases. It can be seen the velocity vectors and contours were well reproduced by the linear theory, such as the 'quiescent area' in Test 9, the curved flow between the moving segments in Test 15, and the half-elliptical velocity distribution in Test 28. The predicted free surface shape also agreed well with the one recorded in the experiment, indicating a high linearity.

For each case, an imaginary velocity probe was set at the centre of the moving bed at a depth equal to $h/2$ (red stars in Fig. 20) for the validation of the velocity histories. A vertical section was set through the probe, for the validation of the velocity distributions at $t = 0.2$ s
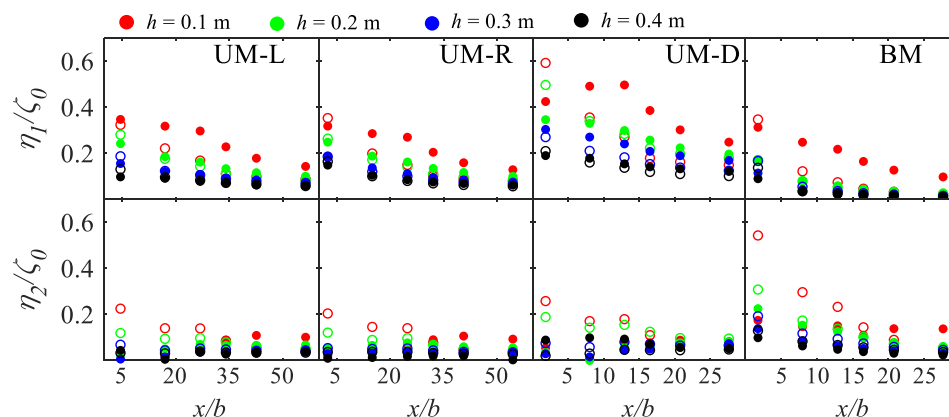

Fig. 15. The normalized η_1 and η_2 for all 32 tests (solid markers denote crest-leading cases and hollow markers denote trough-leading cases).
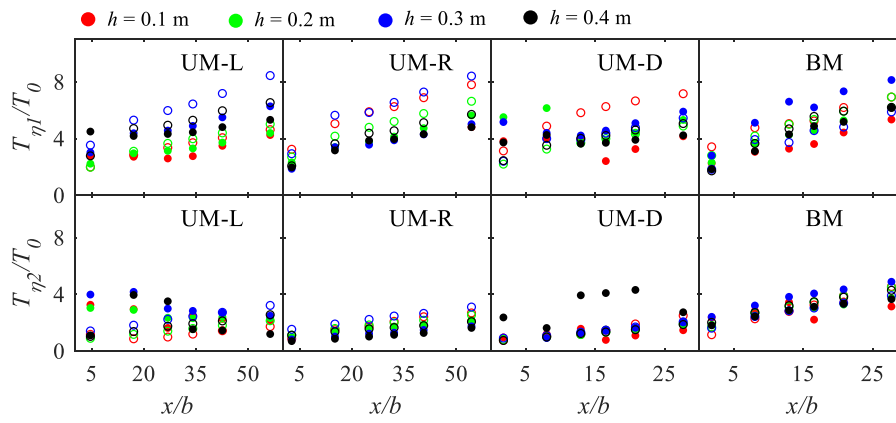
Fig. 16. The normalized $T_{\eta1}$ and $T_{\eta2}$ for all 32 tests (solid markers denote crest-leading cases and hollow markers denote trough-leading cases).
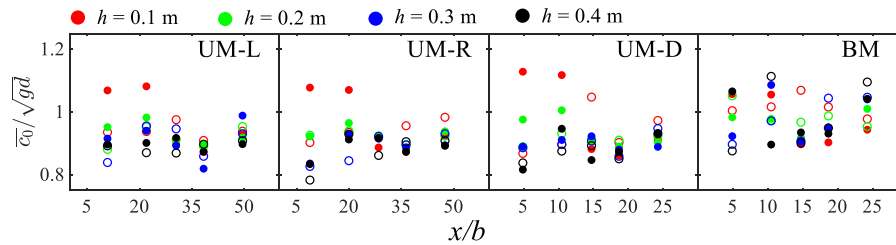

Fig. 17. The normalized propagation speed of the leading extrema for all 32 tests (solid markers denote crest-leading cases and hollow markers denote trough-leading cases).
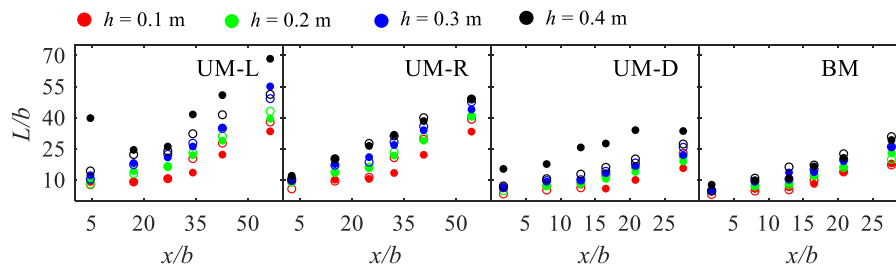

Fig. 18. The normalized wavelength of the leading wave for all 32 tests (solid markers denote crest-leading cases and hollow markers denote trough-leading cases).

(approximately the instant at half-way through the bed movement). For both experimental data and analytical solutions, some velocity components were negligible (of the order of 10^{-4} m/s) at the probes and through the vertical sections, such as the horizontal velocities in Tests 9 and 28 and the vertical velocities in Test 15.

Fig. 21 presents comparisons of the observed and predicted velocity histories at the probes (vertical velocity for Test 9 and 28, horizontal velocity for Test 15) and the velocity distributions at the sections. As shown in Fig. 21, there is very good agreement in the two unimodal cases (Test 9 and 28). However, for the bimodal case (Test 15), the magnitude of the velocity at the probe was slightly underestimated, and the agreement on the velocity distribution was not good. Several factors contributed to this disagreement in Test 15, including: (1) in the experiment the two bed segments did not move purely anti-symmetrically, with the left bed segment not elevating the full 0.05 m. This can be observed from the asymmetric scalar map in the left panel of the middle row of Fig. 20; (2) the opposing movement of the bed segments introduced a stronger wave-wave interaction; (3) the bed
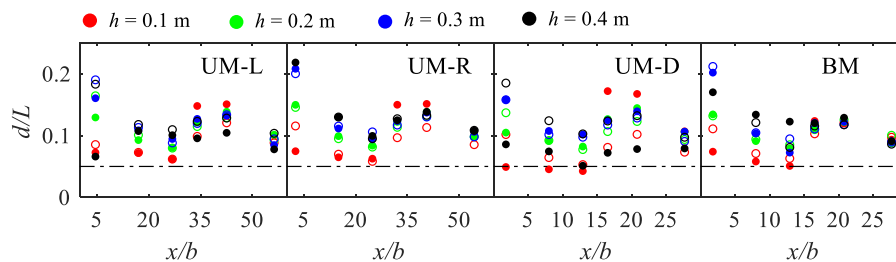

Fig. 19. The ratio of d/L for the leading wave of the 32 tests (solid markers denote crest-leading cases and hollow markers denote trough-leading cases, dashed horizontal line marks the shallow water wave threshold).
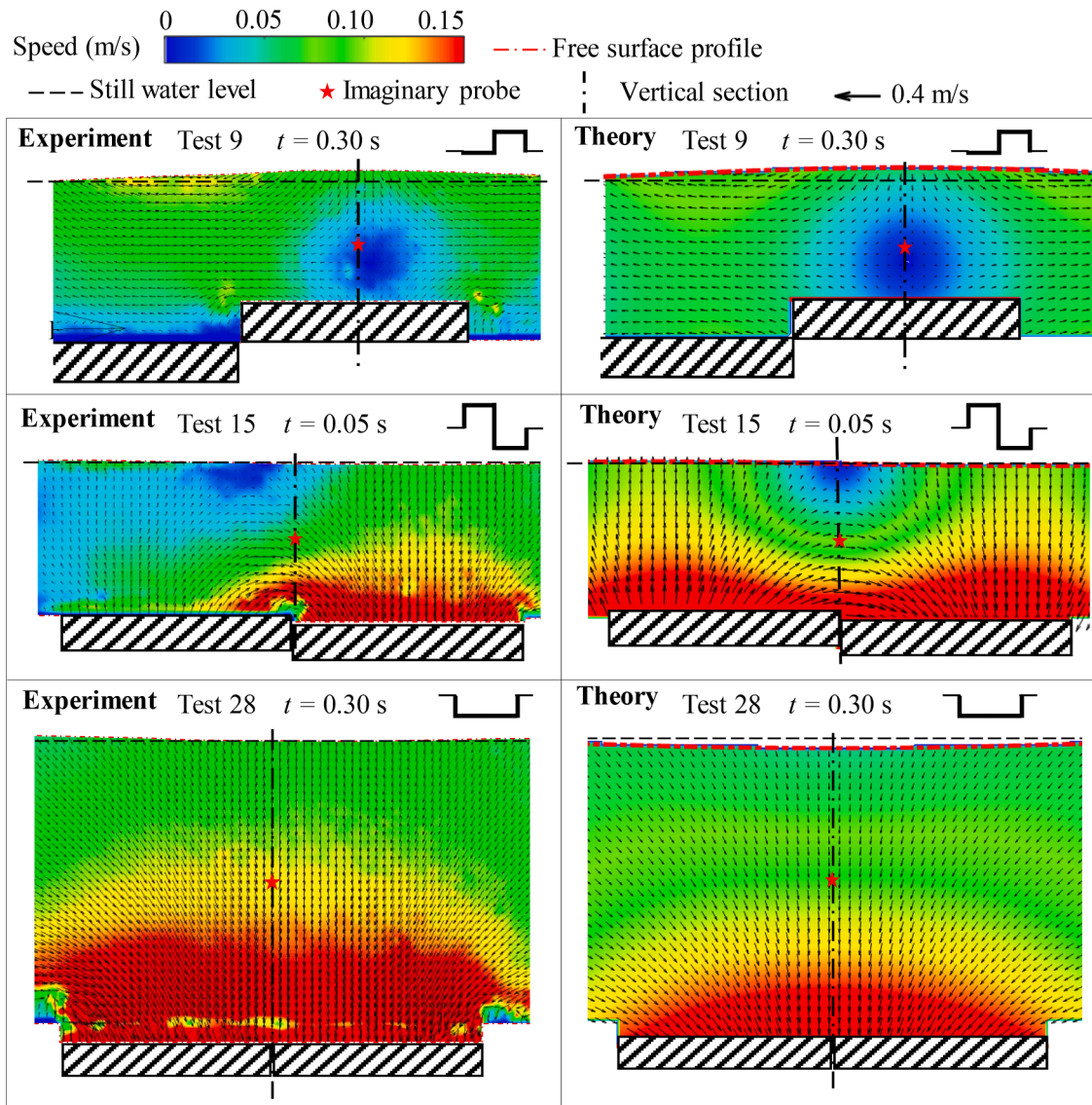
Fig. 20. Free surface profiles, vector maps and isotachs for the experimental data (left column) and analytical solutions (right column) of Tests 9, 15 and 28 at specific time instants.

movements resulted in the local still water depths on the left and right boxes becoming 0.15 m and 0.25 m, respectively. Such a large difference in still water depths amplified the local water flow towards the right box, and introduced a strong non-linearity.

4.2.2. Wave elevation histories

The wave elevation histories for the gauges in region 1 were reproduced by the linear solutions (Eqs. (5) and (6)), exhibiting good agreements with the experimental data for cases with $\alpha \leq 0.25$. For example, Fig. 22 compares the analytical results and experimental measurements at WG3 and WG4, for Tests 12, 13, 16 ($\alpha = 0.25$) and Tests 28, 29, 32 ($\alpha = 0.125$), covering crest-leading cases and trough-leading cases. As shown in Fig. 22, the linear theory predicted the timing, magnitude and decay of the first extrema for both unimodal and bimodal cases very well. However, the second extrema were only well reproduced for bimodal cases.

We adopted Nash Sutcliffe Efficiency Coefficient (E_{NS}) to measure the deviation of the predicted values from the one-to-one relationship with the observations. E_{NS} is a frequently used index in hydrology (Nash and Sutcliffe, 1970), whose definition is:

$$E_{NS} = \frac{\sum_{i=1}^{N} \left(\eta_p - \overline{\eta_o}\right)^2}{\sum_{i=1}^{N} \left(\eta_o - \overline{\eta_o}\right)^2} \tag{9}$$

in which η_p, η_o and $\overline{\eta_o}$ represent the predicted, observed and mean value of the observed wave elevations, respectively, and N is the number of observations. An E_{NS} value of unity describes a perfect match, a zero value means the model predictions are as accurate as the mean of the observed data, while a negative value indicates a less satisfactory prediction (van Bergeijk et al., 2019). Fig. 23 presents the values of E_{NS} of each test at WG3, WG4 and WG5 between t_a (wave arrival time) to $t_a +$ 3.5 s (a duration roughly twice the period of the leading wave cycles, thus $N = 350$). For tests with $\alpha \leq 0.25$, the averaged values of E_{NS} at WG3, WG4 and WG5 were 0.726, 0.709 and 0.715, respectively, indicating a good match. In contrast, for tests with $\alpha = 0.5$, the averaged values of E_{NS} were 0.588, -0.045 and -0.412 at these three wave gauges, revealing a larger discrepancy with linear theory moving from WG3 to WG5. Comparing UM-L/UM-R tests with UM-D tests, it was found the performance of linear theory was reduced insignificantly at a larger disturbance-size scale (δ). BM tests showed slightly larger values of E_{NS} than UM tests, demonstrating a slightly better performance of linear
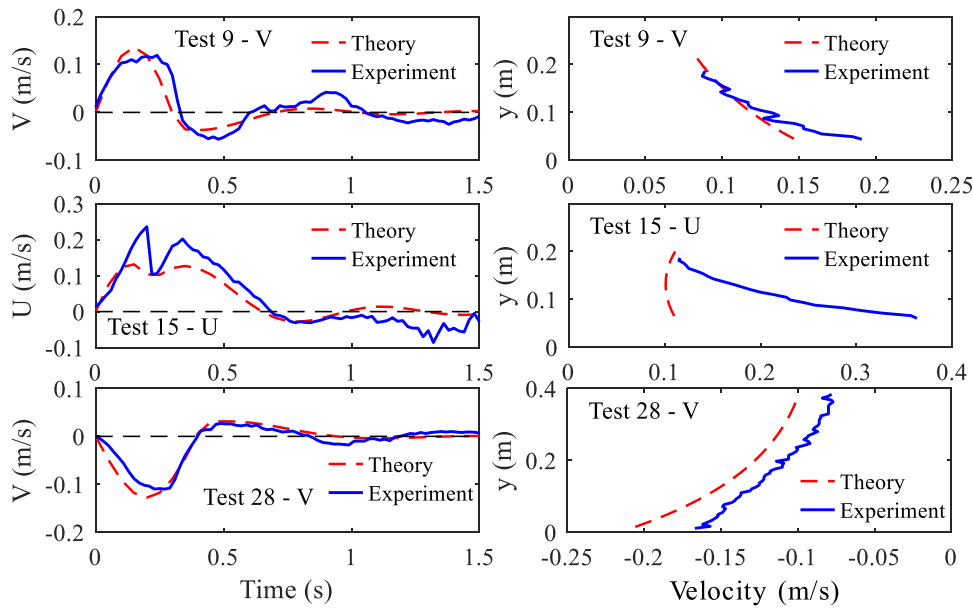
Fig. 21. Left column: The velocity histories of Tests 9, 15 and 28 at the velocity probes; Right column: the velocity distributions of Tests 9, 15 and 28 at t = 0.2 s along the vertical sections.
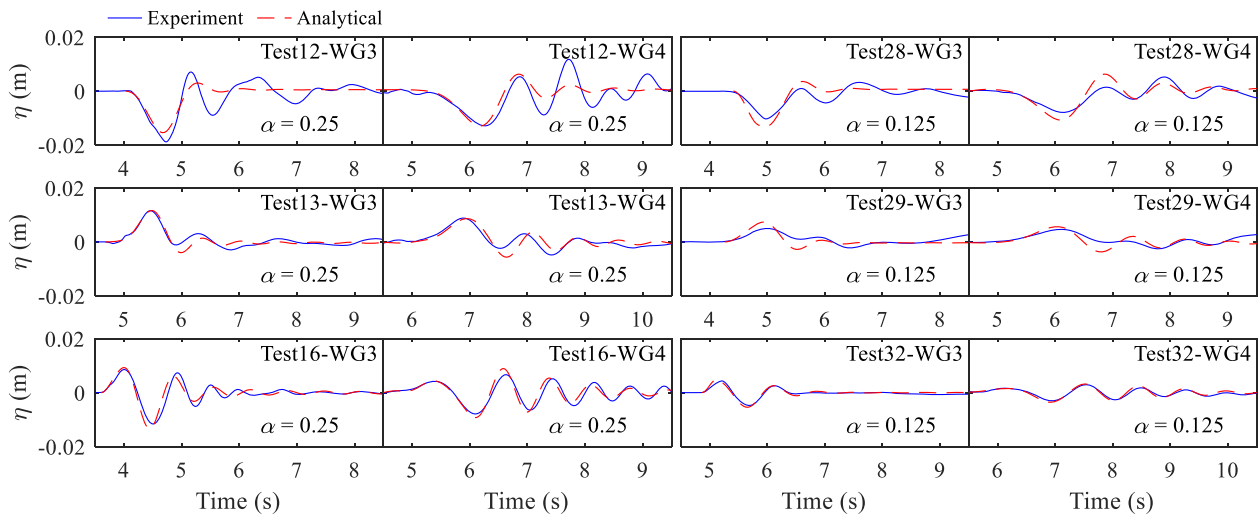

Fig. 22. Analytical solutions and experimental measurements of the surface elevation at WG3 and WG4 for Tests 12, 13, 16 ($\alpha = 0.25$) and Tests 28, 29, 32 ($\alpha = 0.125$).

theory. For our experiment, the time-size parameter $t_c \sqrt{gh} /b$ lay in the range of (0.69, 1.7), indicative of intermediate bed movements (see Section 2.3). The good agreement between experiment and theory in the cases for $\alpha \leq 0.25$ indicates that it is not necessary to restrict the time-size parameter to be $>> 1$ or $<< 1$ for the application of linear theory.

Fig. 24 compares the predicted amplitudes of the first two leading extrema with the experimental data for all 32 tests. As shown in Fig. 24, there is generally a good match for the amplitude of the first extremum (α in the range of [0.125, 0.5]). However, a good agreement on the second extremum is only achieved for cases with $\alpha \leq 0.25$. When $\alpha = 0.5$ the linear solutions overestimated the amplitude of second extremum of the crest-leading cases and underestimated it in trough-leading cases.

According to the validations on the flow field, wave elevation histories and amplitudes of wave extrema, the following conclusions can be made:

- the disturbance-amplitude scale (α) was the most crucial factor dominating the linearity of the generated wave train, compared to the disturbance-size scale (δ) and time-size parameter ($t_c \sqrt{gh}/b$);
- when $\alpha \leq 0.25$, the linear solution can well predict the waves generated by the 'intermediate' bed movement type, and it was not necessary to restrict the time-size parameter to be $>> 1$ or $<< 1$ for the application of linear theory;
- when $\alpha \geq 0.5$, the nonlinear response became significant in the wave generation and propagation, which cannot be well represented by the linear theory. However, the linear theory can still reasonably predict the amplitude of the first extrema in the area close to the moving bed.

4.3. Non-linear behaviour

4.3.1. Wave generation in shallow water
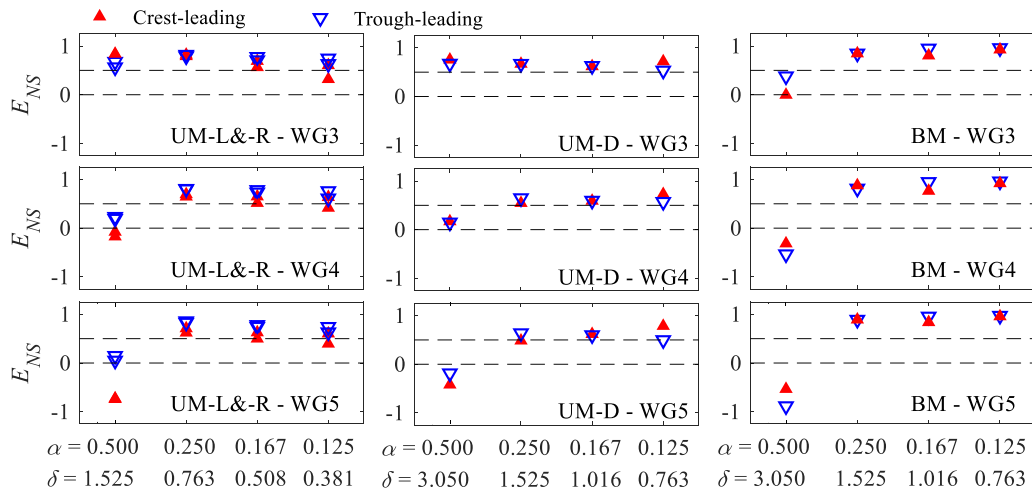The strong non-linearity in the cases with $\alpha = 0.5$ led to different

Fig. 23. Nash Sutcliffe Efficiency Coefficient (E_{NS}) of the predicted wave elevation histories at WG3, WG4 and WG5 for all tests (the two black dashed lines stand for ($E_{NS} = 0$ and $E_{NS} = 0.5$, respectively).
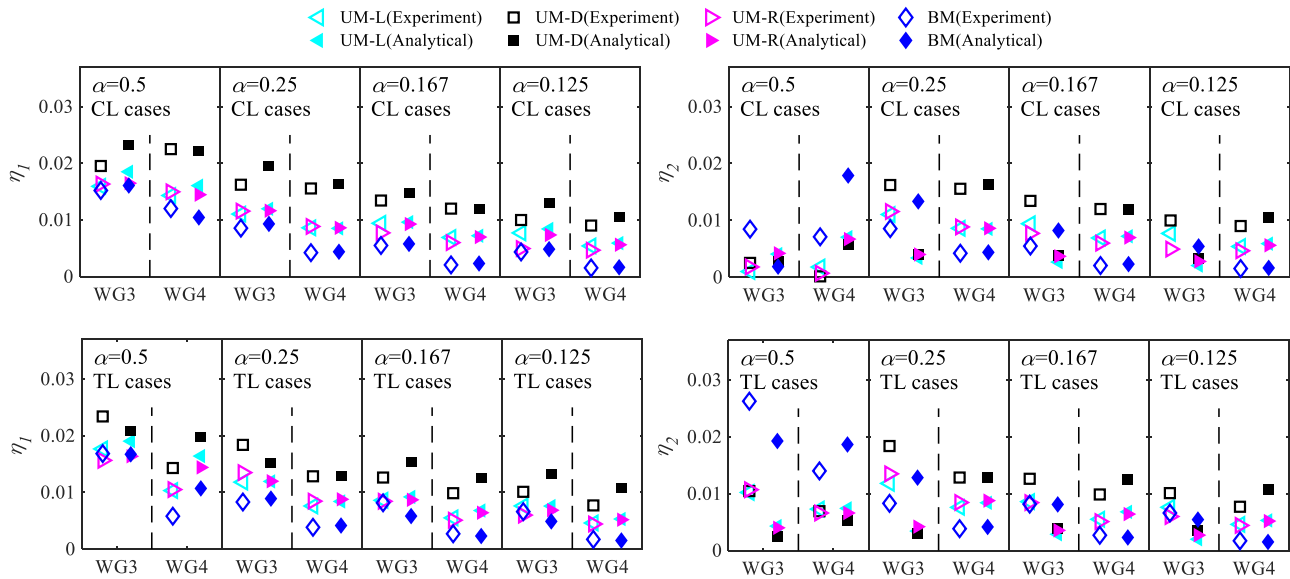

Fig. 24. The comparison between experimental data and analytical solutions of the first two leading extrema at WG3 and WG4 for all cases.

responses for crest-leading and trough-leading wave trains. As shown in Figs. 11 to 13, when $\alpha = 0.5$, an upward unimodal bed motion resulted in a crest-leading wave, resembling a solitary wave with a remarkably stable crest (η_1) followed by a string of very modest surface disturbances. Conversely, when the bed moved downwards, an unimodal motion generated a trough-leading wave, exhibiting notable differences from a solitary wave. The trough-leading wave trains quickly transformed into a leading trough (η_1) followed by a regular wave train with amplitude similar to η_1. The same pattern was also evident in the bimodal cases with $\alpha = 0.5$, as seen in Fig. 14. The leading extremum was stable for the crest-leading cases, and the trough-leading waves quickly transformed into a non-dispersive solitary wave followed by a periodic wave train while travelling from WG3 to WG5. Interestingly, this form of behaviour was predicted by the linear analysis of Braddock et al. (1973). Also noteworthy is that trough-leading waves resulting from a bimodal bed movement showed a very steep wave crest (η_2), which was more significant when $\alpha = 0.5$ (Test 7), compared to that when $\alpha = 0.25$ (Test 15).

As α approached O (1), nonlinear effects became more pronounced, and the bed movement significantly changed the local water depth,

leading to a stronger fluid response in the wave generation area. For example, Fig. 25 compares the snapshots of experimental data and analytical results of the unimodal cases with the left bed segment moving for $\alpha = 0.5$ (rows 1 and 2 for Test 5, and rows 3 and 4 for Test 6). For both upward and downward movements, the analytical results agree well with the experimental data on the amplitude of η_1 and the corresponding flow field. However, discrepancies appeared afterward. The uplifted bed segment in Test 5 reduced the still water depth by about 50 %, and hampered the downward movement of water during the adjustment under gravity, leading to a reduction in the amplitude of η_2 (see the scalar map at $t = 0.75$ s of Test 5 in Fig. 25). In contrast, in the case of a falling bed segment (Test 6), the experimental data shows a larger amplitude of η_2, with the surrounding water filling the rupture at a greater rate than predicted (see the scalar maps at $t = 0.30$ s of Test 6 in Fig. 25). The rapid inward flows converged above the centre of the moving bed to form a large bore over the bed rupture (see the scalar map at $t = 0.55$ s of Test 6 in Fig. 25). However, the free surface predicted by analytical solutions did not exceed the still water level, indicating the strengthened non-linear effects with a larger α. Moreover, due to the limitation of the linear theory, the vortices recorded in the experiment
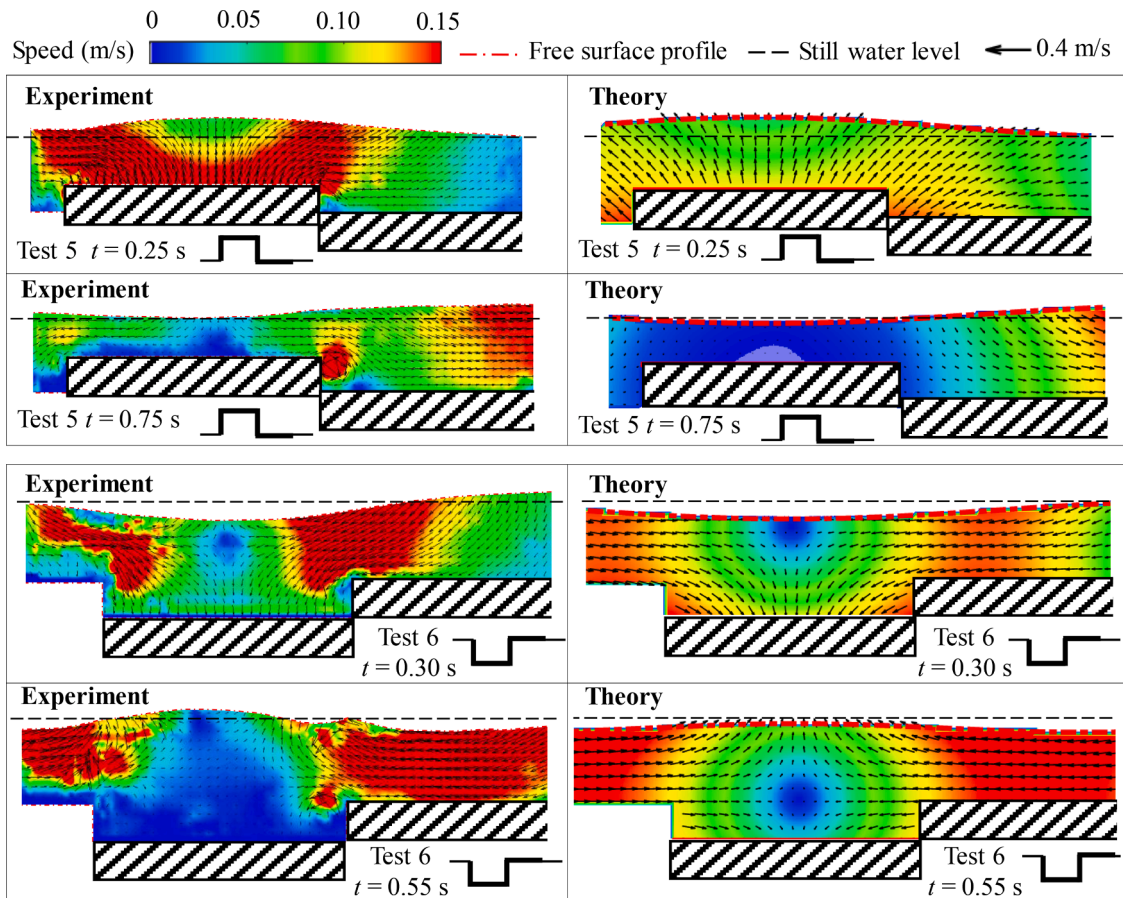
Fig. 25. Free surface profiles, vector maps and isotachs of the velocity field for Tests 5 ($h = 0.1$m, rows 1 and 2) and 6 ($h = 0.1$m, rows 3 and 4). Rows 1 and 3 show the formation of the first extrema (η_1) and rows 2 and 4 show the formation of the second extremum (η_2).

cannot be reproduced by the analytical solutions. In the second row of the left column of Fig. 25, vortices can be observed at both edges of the uplifted segment, with the right one being more pronounced. This was because the uplifted segment obstructed the high-speed camera's view, shadowing the flow field immediately to the left of the segment.

Bimodal cases exhibited stronger wave-wave interaction and flow mixing than unimodal cases when $\alpha = 0.5$. Taking Test 8 as an example, Fig. 26 compares the free surface profiles and flow fields recorded by the PIV with the analytical results at distinct instants. Significant discrepancies are evident beyond $t = 0.50$ s, at which stage a bore was formed on the left segment. Wave breaking occurred in the experiment at $t = 0.70$ s, together with an intense local vortex. Due to the nonlinear wave-wave interactions and inertia effects, the wave train generated by bimodal movement cannot be regarded as the superposition of the wave trains generated by two single unimodal movements with opposite directions (UM-L and UM-R).
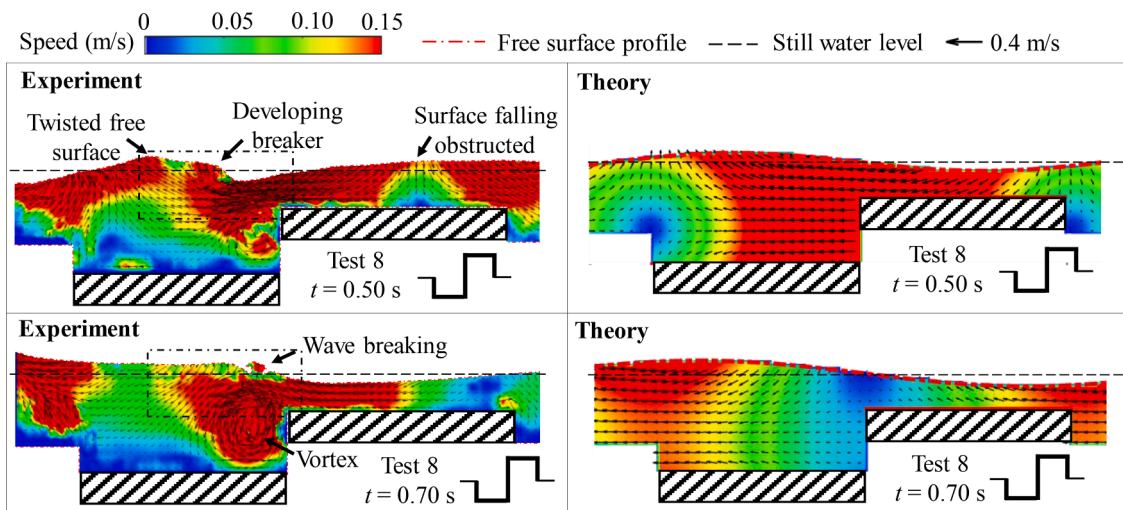

Fig. 26. Free surface profiles, vector maps and isotachs of the velocity field for Test 8 ($h = 0.1$ m, BM-CL; the dash-dotted boxes in the left panel indicate the observation window of Fig. 27).
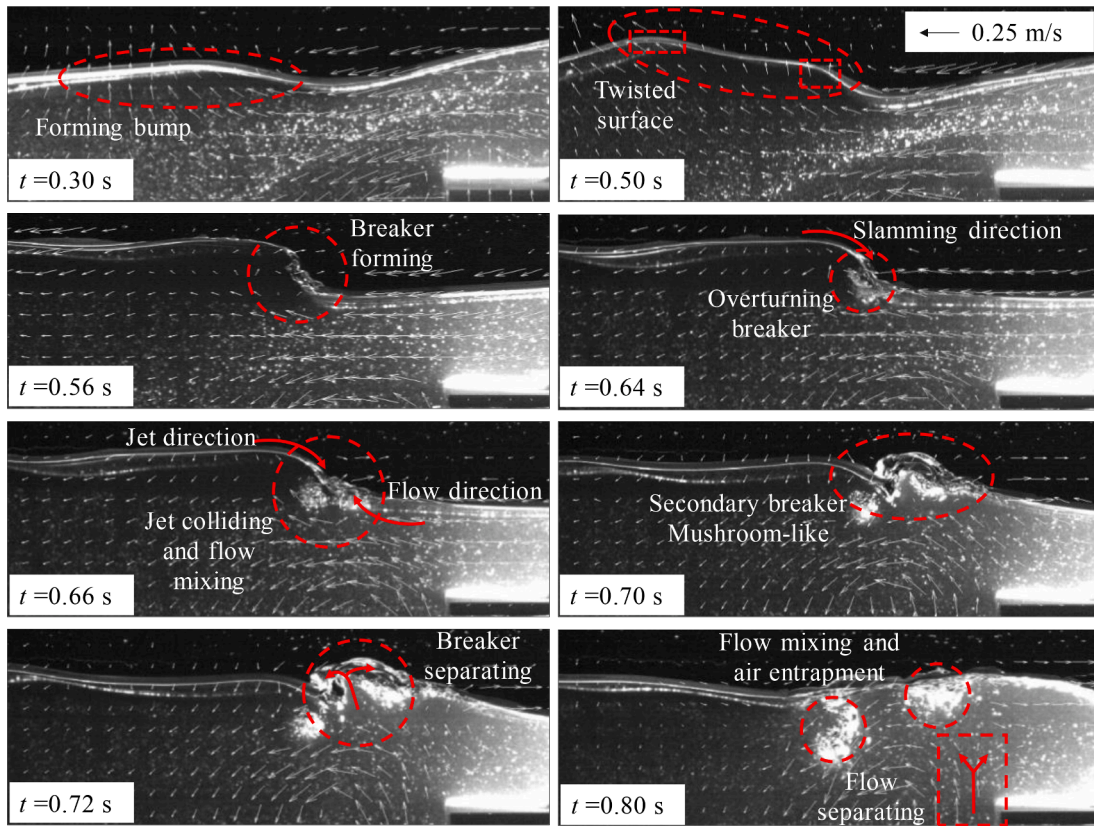
Fig. 27. The free surface and vector map of the breaking wave in the wave generation area (For a clear view the scalar maps are removed, the observation window is shown in Fig. 26).

4.3.2. Breaking wave in the generation area

Further details of Test 8 are presented in Fig. 27, depicting the flow fields around the juncture of the moving beds between $t = 0.30$ s and $t = 0.80$ s. At $t = 0.30$ s and 0.50 s, the leftward flow from the uplifted segment was much faster than the flow above the downthrust segment,

leading to a large velocity gradient. Two local high points may be observed on the twisted surface at $t = 0.50$ s (red-dashed boxes in Fig. 27, top-right panel), in which the left one originated from the overfilling above the downthrust segment, and the right one resulted from the local high velocity gradient causing the rise of the local free
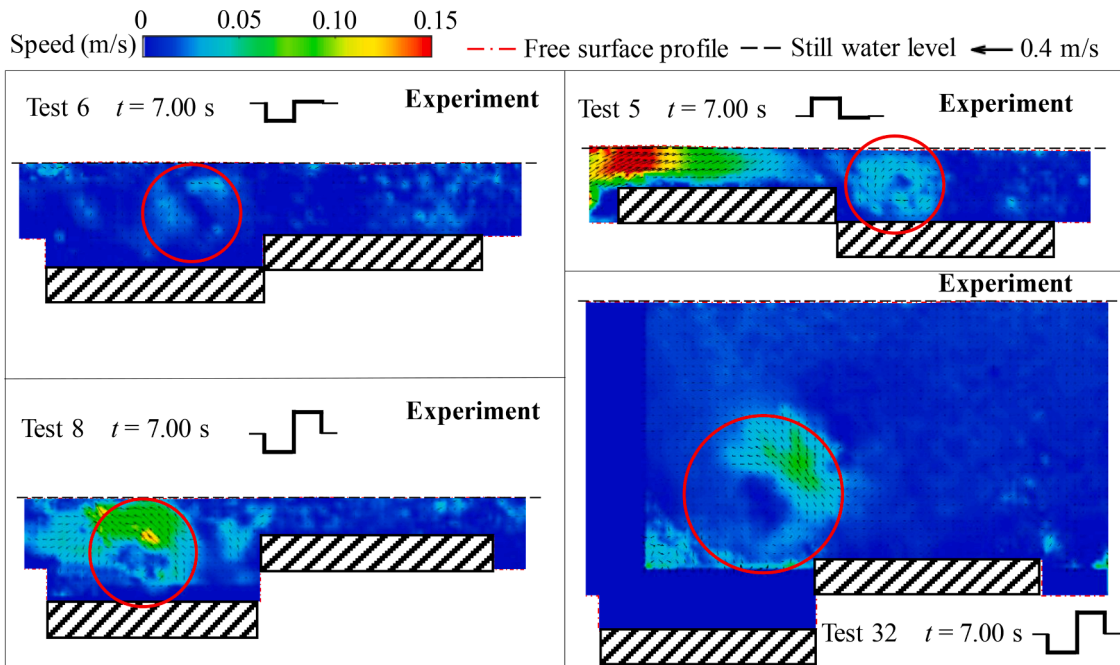

Fig. 28. Free surface profiles, vector maps and isotachs of the velocity field derived from PIV measurements for Tests 5, 6, 8 and 32 at $t = 0.70$ s.

surface. Around the juncture of the two segments, the falling concave surface induced a reduction of the local water level over the right segment, and the developing crests led to an increasing water level over the left segment. Their combined effect resulted in a near-vertical free surface at $t = 0.56$ s, forming a local breaker propagating towards the right at $t = 0.64$ s. The breaker then encountered the leftward flow (resulting from the gravitational adjustment of the concave bulge above the righthand bed segment), leading to an intensive mixing of water and air ($t = 0.66$ s). Subsequently, the interaction of these opposing flows generated a secondary breaker shaped like a mushroom ($t = 0.70$ s), which separated towards both right- and left-hand sides ($t = 0.72$ s), leading to a more intensive water and air mixing ($t = 0.80$ s). At this stage, air entrapment was observed and there was a flow separation visible at the juncture of the two bed segments. Although this wave breaking had little effect on the magnitude of the first two rightward propagating extrema, it did dampen the energy in the following wave train.

4.3.3. Long-lasting vortex

Closed vortices were observed for both unimodal and bimodal cases, at the borders of the uplifted or fallen segments. The vortices were not fully established until the second extrema had left the wave generation area. Subsequently, the vortices expanded slowly and moved away from the higher bed segment, with the radius eventually becoming comparable with ζ_0. Fig. 28 presents the flow field at $t = 7.0$ s, for Tests 5, 6, 8 and 32. It can be seen that the vortices (in the red circles) persisted for a long time (longer than $20T_0$), and the flow speeds of the vortices reduced with the water depth, and they were more pronounced in bimodal cases than in the unimodal ones. The analytical solutions based on potential flow theory, described in Section 3, are unable to describe rotational flow phenomenon such as these long-lasting vortices.

4.3.4. Ursell number

For an estimation of the wave nonlinearity, we examined the Ursell number (Ursell, 1953) of the leading wave at each of the wave gauges for all tests. The Ursell number (Ur) can be calculated as HL^3/h^3, in which H denotes the wave height, L the wavelength and h the local water depth (Phan et al., 2019; Yin et al., 2021). Here, we adopt the criterion proposed by Heller and Ruffini (2023), that waves with Ur larger than 26 involve noticeable non-linearity. Fig. 29 shows the local Ursell number of the leading wave at each wave gauge. The nonlinearity grows as the water depth reduces. The majority of the waves exhibit Ur values below 10, suggesting low non-linearity. Only instances with $\alpha = 0.5$ surpass the Ur threshold of 26, indicating a high degree of non-linearity. Comparing the unimodal cases at a fixed water depth (Fig. 29), the cases with both moving bed segments (UM-D) show larger Ur values than those with a single moving bed segment (UM-L and UM-R). This suggests that nonlinearity increases with the size of the moving bed segment. The Ursell number of the waves generated by different bed movement modes show similar trends during the propagation; that the nonlinearity grows as the waves propagate on a flatbed, (WG3 to WG5 and WG7 to WG8),

while it reduces where the water depth increases between WG5 to WG7.

5. Conclusion

In this paper, we have investigated the generation and propagation of wave trains created by vertical bed movements with 'intermediate' speed. Unimodal and bimodal seabed movements were explored, with disturbance-amplitude scales (α) varying between 0.125 and 0.5, and disturbance-size scales (δ) varying between 0.38 and 3.05. A PIV system was used to provide observations of fluid velocities in the vicinity of the wave generation area.

It was found α is the most crucial factor dominating the linearity of the wave trains. For $\alpha \leq 0.25$, the dynamics were strongly linear and flow was laminar. For example, very good agreement was found between the mirror images of the trough-leading wave trains and their crest-leading counterparts. A unimodal bed movement led to a solitary-like leading wave with a significant initial peak/trough followed by a wave train with much lower amplitudes. The magnitudes of the initial peak/trough or trough/peak combination generated by a bimodal bed movement were similar. For $\alpha \geq 0.5$, non-linearity became more pronounced. Wave breaking and air entrainment were observed in the wave generation area. There was poor agreement between the mirror images of the trough-leading wave trains and their crest-leading counterparts. For a crest-leading wave train, the amplitude and shape of the solitary leading wave were well maintained when propagating, and the following wave train was not well-defined. For a trough-leading wave train the leading trough decayed significantly when propagating, and was followed by a sequence of well-defined regular waves. For all cases we have explored, the leading extrema of the wave train decayed noticeably, almost disappearing after propagating over a large distance, with the following regular wave train growing in significance. This phenomenon has also been observed in real-world tsunami events. Long-lasting vortices were observed in the wave generation area for all cases and may contribute to the energy dissipation of the following wave trains.

New linear solutions for the velocity potential of fluid flow in response to unimodal and bimodal bed movements have been presented, enabling the calculation of the corresponding velocity fields. For $\alpha \leq 0.25$, the observed flow fields and wave histories were in very good agreement with linear theory. We found that the applicability of linear theory did not require the time-size parameter ($t_c \sqrt{gh}/b$) to be $>> 1$ or $<< 1$ as proposed by Hammack (1972). For $\alpha \geq 0.5$, the application of linear theory was highly limited, and it was only capable of giving a moderately good estimate of the amplitude of the first extremum in the area close to the moving bed.

In conclusion, this paper has presented new experimental and analytical results for wave trains generated by segmented vertical seabed movements, providing the basis for the exploration of more complex situations in the future.
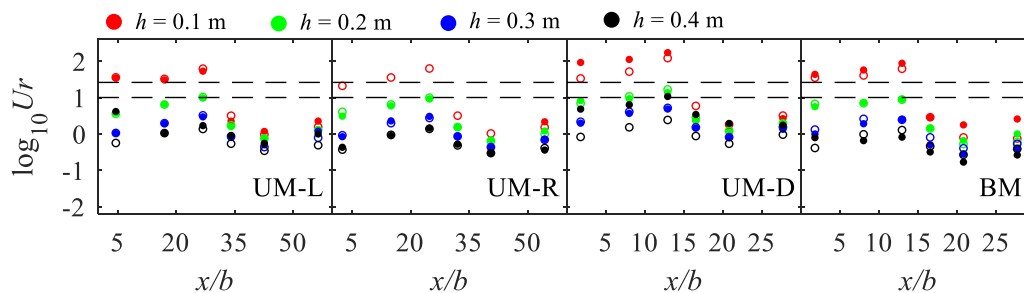

Fig. 29. Local Ursell numbers of the leading wave from WG3 to WG8 evaluated from the experimental data of all 32 tests (solid markers denote crest-leading cases and hollow markers denote trough-leading cases, dashed lines denote the thresholds for $Ur = 10$ and $Ur = 26$)

CRediT authorship contribution statement

Dominic E. Reeve: Writing – review & editing, Supervision, Project administration, Methodology, Funding acquisition. **Jose Horrillo-Caraballo:** Writing – review & editing, Investigation. **Harshinie Karunarathna:** Writing – review & editing, Supervision. **Xin Wang:** Writing – original draft, Methodology, Investigation, Data curation.

Declaration of competing interest

The authors declare that they have no known competing interests or personal relationships that could have appeared to influence the work reported in this paper.

Data availability

Data will be made available on request.

References

Allan, J.C., Komar, P.D., Ruggiero, P., Witter, R., 2012. The March 2011 Tōhoku tsunami and its impacts along the US west coast. J. Coast. Res. 28 (5), 1142–1153.

Braddock, R.D., Van Den Driessche, P., Peady, G.W., 1973. Tsunami generation. J. Fluid Mech. 59 (4), 817–828.

Das, S., Meylan, M.H., 2023. Time-domain wave response of a compressible ocean due to an arbitrary ocean bottom motion. Appl. Math. Model. 118, 832–852.

Enet, F., Grilli, S.T., 2007. Experimental study of tsunami generation by three-dimensional rigid underwater landslides. J. Waterw. Port. Coast. Ocean. Eng. 133 (6), 442–454.

Fuhrman, D.R., Madsen, P.A., 2009. Tsunami generation, propagation, and run-up with a high-order Boussinesq model. Coast. Eng. 56 (7), 747–758.

Hammack, J.L., (1972). Tsunamis—a model for their generation and propagation, W.M. Keck Laboratory of Hydraulics and Water Resources, California Institute of Technology, Pasadena, California, Report No. KH-R-28.

Hayir, A., 2004. Ocean depth effects on tsunami amplitudes used in source models in linearized shallow-water wave theory. Ocean Eng. 31 (3-4), 353–361.

Heller, V., Ruffini, G., 2023. A critical review about generic subaerial landslide-tsunami experiments and options for a needed step change. Earth Sci. Rev., 104459

Jamin, T., Gordillo, L., Ruiz-Chavarría, G., Berhanu, M., Falcon, E., 2015. Experiments on generation of surface waves by an underwater moving bottom. Proc. R. Soc. A Math. Phys. Eng. Sci. 471 (2178), 20150069.

Lu, H., Park, Y.S., Cho, Y.S., 2017. Modelling of long waves generated by bottom-tilting wave maker. Coast. Eng. 122, 1–9.

Lynett, P.J., Wu, T.R., Liu, P.L.F., 2002. Modeling wave runup with depth-integrated equations. Coast. Eng. 46 (2), 89–107.

Madsen, P.A., Fuhrman, D.R., Schäffer, H.A., 2008. On the solitary wave paradigm for tsunamis. J. Geophys. Res. Oceans 113 (C12).

Maeda, T., Furumura, T., Sakai, S.I., Shinohara, M., 2011. Significant tsunami observed at ocean-bottom pressure gauges during the 2011 off the Pacific coast of Tohoku Earthquake. Earth Planets Space, 63, 803–808.

Merrifield, M.A., Firing, Y.L., Aarup, T., Agricole, W., Brundrit, G., Chang-Seng, D., Farre, R., Kilonsky, B., Knight, W., Kong, L., Magori, C., Manurung, P., McCreery, C., Mitchell, W., Pillay, S., Schindele, F., Shillington, F., Testut, L., Wijeratne, E.M.S., Caldwell, P., Jardin, J., Nakahara, S., Porter, F.Y., Turetsky, N., 2005. Tide gauge observations of the Indian Ocean tsunami, December 26, 2004. Geophys. Res. Lett. 32 (9).

Nash, J.E., Sutcliffe, J.V., 1970. River flow forecasting through conceptual models part I—A discussion of principles. J. Hydrol. 10 (3), 282–290.

Phan, K.L., Stive, M.J.F., Zijlema, M., Truong, H.S., Aarninkhof, S.G.J., 2019. The effects of wave non-linearity on wave attenuation by vegetation. Coast. Eng. 147, 63–74.

Pinet, P.R., 2019. Invitation to Oceanography. Jones & Bartlett Learning, Sudbury (MA).

Rossetto, T., Allsop, W., Charvet, I., Robinson, D.I., 2011. Physical modelling of tsunami using a new pneumatic wave generator. Coast. Eng. 58 (6), 517–527.

Satake, K., Tanioka, Y., 1999. Sources of tsunami and tsunamigenic earthquakes in subduction zones. Pure Appl. Geophys. 154, 467–483.

Satake, K., Fujii, Y., Harada, T., Namegaya, Y., 2013. Time and space distribution of coseismic slip of the 2011 Tohoku earthquake as inferred from tsunami waveform data. Bull. Seismol. Soc. Am. 103 (2B), 1473–1492.

Sato, M., Ishikawa, T., Ujihara, N., Yoshida, S., Fujita, M., Mochizuki, M., Asada, A., 2011. Displacement above the hypocenter of the 2011 Tohoku-Oki earthquake. Science 332 (6036), 1395.

Schimmels, S., Sriram, V., Didenkulova, I., 2016. Tsunami generation in a large scale experimental facility. Coast. Eng. 110, 32–41.

Shen, Y., Whittaker, C.N., Lane, E.M., Power, W., Melville, B.W., 2022. Interference effect on tsunami generation by segmented seafloor deformations. Ocean Eng. 245, 110244.

Slatt, R.M., 2013. Nondeltaic, shallow marine deposits and reservoirs. In: Developments in Petroleum Science, 61. Elsevier, pp. 441–473.

Synolakis, C.E., Bernard, E.N., 2006. Tsunami science before and beyond boxing day 2004. Philos. Trans. R. Soc. A Math. Phys. Eng. Sci. 364 (1845), 2231–2265.

Tjandra, S.S., Pudjaprasetya, S.R., 2015. A non-hydrostatic numerical scheme for dispersive waves generated by bottom motion. Wave Motion. 57, 245–256.

Ursell, F., 1953. The long-wave paradox in the theory of gravity waves. In: Proceedings of the Mathematical Proceedings of the Cambridge Philosophical Society, 49. Cambridge University Press, pp. 685–694.

van Bergeijk, V.M., Warmink, J.J., van Gent, M.R.A., Hulscher, S.J.M.H., 2019. An analytical model of wave overtopping flow velocities on dike crests and landward slopes. Coast. Eng. 149, 28–38.

Wang, X., Liu, P.L.F., 2006. An analysis of 2004 Sumatra earthquake fault plane mechanisms and Indian Ocean tsunami. J. Hydraulic Res. 44 (2), 147–154.

Whittaker, C.N., Nokes, R.I., Lo, H.Y., Liu, P.F., Davidson, M.J., 2017. Physical and numerical modelling of tsunami generation by a moving obstacle at the bottom boundary. Environ. Fluid Mech. 17 (5), 929–958.

Yim, S.C., Yuk, D., Panizzo, A., Di Risio, M., Liu, P.F., 2008. Numerical simulations of wave generation by a vertical plunger using RANS and SPH models. J. Waterw. Port. Coast. Ocean. Eng. 134 (3), 143–159.

Yin, K., Xu, S., Gong, S., Zhou, R., Wang, Y., 2021. Effects of wave nonlinearity on submerged flexible vegetation dynamics and wave attenuation. Ocean Eng. 241, 110103.